Fast neural network-based direct simulation Monte Carlo solutions of shock flow of diatomic gases with vibrational modes

Gagan Garg (गगन गर्ग)[a], Tapan K. Mankodi (तपन के मंकोड़ी)[b], Rho Shin Myong (명노신)[a),1)]

[a)] School of Mechanical and Aerospace Engineering and ACTRC, Gyeongsang National University, Jinju, Gyeongnam 52828, South Korea

[b)] Department of Mechanical Engineering, Indian Institute of Technology Guwahati, Guwahati 781039, India

Abstract: A novel way to solve gas flows in thermal non-equilibrium has been proposed by Garg *et al*. (*Physics of Fluids*, 106113, 2024), which built compact constitutive relations for monatomic gases in advance by applying deep neural network (DNN) machine learning (ML) to available direct simulation Monte Carlo (DSMC) solution data, and later combined them with the conventional finite volume method (FVM) for the physical laws of conservation. We extend this FVM-DSMC-ML framework to diatomic gases by employing the two-temperature framework (translational and rotational) as well as the three-temperature framework (translational, rotational, and vibrational), coupled with DNN-based DSMC constitutive relations for viscous stresses and heat fluxes associated with these energy modes. After resolving challenges associated with various energy modes, we evaluate the performance of the FVM-DSMC-ML solver for diatomic gases for the compressive shock structure problem. Developing a successful DNN model requires the careful selection of input and output parameters, as well as meticulous attention to the details of various DNN parameters. The DNN model of DSMC constitutive relations is trained using filtered data as inputs, with corresponding DSMC data as outputs. The study demonstrates that the FVM-DSMC-ML solver provides results in excellent agreement with the actual DSMC solutions and shows superior performance, with its computational cost being 1/50 of that of the conventional DSMC solver. The DSMC topologies reveal pronounced nonlinearities and strong coupling between viscous stresses and heat fluxes, and for the most part they exhibit higher values of viscous stress and heat fluxes compared to the NSF topology.

Keywords: Rarefied and microscale diatomic gases; deep neural network; DSMC; constitutive relations; finite volume method; shock wave structure

[1)] Corresponding author: Tel: +82-55-772-1645. Email: myong@gnu.ac.kr.

I. INTRODUCTION

The advent of high-speed space vehicles flying at the edge of space has created a need to understand several important gas flow phenomena. One of the major areas that has received much attention in recent years is high-temperature (rarefied) gas dynamics. The topic incorporates a great deal of complexity and requires an understanding of gas flow physics at a fundamental level [1-5]. The majority of the Earth's atmosphere consists of diatomic gases (i.e., nitrogen and oxygen), where high-temperature conditions can lead to complex physical phenomena. These include the excitation of molecules to higher vibrational and electronic quantum levels and changes in the structure or identification of molecules that result from chemical reactions and ionization [6-8].

Re-entry vehicles inevitably encounter high-temperature flow situations because of the high-speed flow that surrounds them while flying through the layers of Earth's atmosphere [7-11]. When descending at hypersonic speeds, the vehicles encounter harsh conditions and extreme temperatures, especially in the shock and the post-shock region. Further complications in the flow can result from the rapid increase in rarefaction at high altitudes, resulting in a high degree of non-equilibrium.

For these conditions, conducting full-scale experimental studies, either on the ground or in real flight, would be prohibitively expensive [12]. Thus, computational simulations are often employed to gain a deeper and better understanding of the high-temperature re-entry gas flows. The most widely used numerical methodology involves solving the conservation laws for mass, momentum, and energy in combination with the (first-order) Navier–Stokes and Fourier (NSF) constitutive relations. These, coupled with additional conservation laws for vibration mode and species, have been widely employed to investigate hypersonic flows at lower altitudes (< 55 km) [6, 13-15]. Source terms for the vibrational energy balance and species balance are introduced in the conservation laws to account for the non-equilibrium effects in the trans-rotational and vibrational mode of energy, and the chemical reactions in the flow, respectively. Since the NSF constitutive relations are modeled with the basic assumption that the

flow is near local thermal equilibrium (LTE), their validity becomes questionable for cases where the flow is away from the LTE assumption.

To overcome these limitations, the following Boltzmann kinetic equation (BKE) is often used, which can capture the detailed physics for flows far from thermal non-equilibrium,

$$\left(\frac{\partial}{\partial t}+\boldsymbol{v}\cdot\boldsymbol{\nabla}\right)f\left(\boldsymbol{v},\boldsymbol{r},t\right)=C\left[f,f_2\right]. \tag{1}$$

Here, $f\left(\boldsymbol{v},\boldsymbol{r},t\right)$ and $C\left[f,f_2\right]$ represent the distribution function in terms of the particle velocity, the particle position, and time, and the Boltzmann collision integral, respectively. Direct analytical and numerical solutions of BKE are complex due to the Boltzmann collision term.

An alternative method to obtain an approximate solution of BKE is the direct simulation Monte Carlo (DSMC) [16, 17]. The DSMC method is a statistical technique (not based on any partial differential equation) that decouples the kinematic and collision processes in the original BKE by directly simulating the motion of statistically representative particles and carrying out probabilistic collisions [16-21]. In DSMC, the effects of internal degrees of freedom and chemical reactions are taken into account through inelastic [22, 23] and reactive [16, 24, 25] collision models, respectively. Due to its statistical nature, DSMC is computationally expensive when simulating flow situations at altitudes below 70 km. This limitation of DSMC emanates from the requirement that a large ensemble of particles must be tracked to reduce the statistical noise within the solution.

To address the issue of computational cost associated with DSMC, researchers have been working to develop a hybrid approach that combines DSMC and FVM-NSF frameworks based on the domain decomposition concept [26-28]. However, this method continues to encounter significant limitations compared to the traditional computational fluid dynamics (CFD) method, since DSMC is still handling a portion of the domain. An alternative strategy to mitigate the inherent statistical noise in DSMC simulations—without incurring the substantial computational cost associated with increasing particle numbers—is the implementation of information-preserving (IP) variants of the DSMC method [29, 30].

However, even with these advanced techniques, the overall computational expense remains significantly higher compared to conventional finite volume methods (FVM).

Numerous researchers have also tackled the crucial challenge associated with the direct solution of the Boltzmann kinetic equation (BKE), specifically concerning the collision integral. Their aim is to develop simplified models for this term. Among them, the Bhatnagar-Gross-Krook (BGK) [31], Shakhov-BGK [32], ellipsoidal statistical BGK (ES-BGK) [33], unified stochastic particle BGK (USP-BGK) [34, 35], and Fokker–Planck (FP) [36] approaches represent linearized or simplified Boltzmann model equations [37-41].

Another way is to reduce the original BKE to a set of conservation laws in the form of partial differential equations (PDEs), which can be solved in conjunction with a set of higher-order constitutive relations. Following this approach, researchers have presented various equations called extended or generalized hydrodynamic equations. The extended hydrodynamic equation framework includes Burnett-type equations [42-46], the Grad-13 moment method [47, 48], and the regularized-13 moment method [49, 50]. In another study, based on Eu's generalized hydrodynamic equations [51, 52], Myong [11, 53-60] developed the nonlinear coupled constitutive relations (NCCRs) in algebraic form. These methods provide a distinct advantage in computational efficiency over the previously mentioned particle-based methods but suffer from a disadvantage in accuracy. Specifically, the macroscopic properties predicted by these methods are less accurate than full kinetic solutions, and thus require an ingenious solution methodology to simultaneously exploit the advantages of the DSMC (i.e., correct solution of BKE) and conventional CFD methods (i.e., affordable computational cost).

In recent years, machine learning-based solution strategies have attracted significant attention in the computational physics community. For the problem at hand, these methodologies can broadly be categorized into two paradigms. The first, often referred to as the '*black-box*' approach, involves training deep neural networks (DNNs) to learn and replicate the constitutive relations embedded within DSMC data [1]. The second, a '*white-box*' framework, focuses on the data-driven discovery of governing equations using DSMC-generated datasets [61, 62]. In the present study, we adopt the '*black-box*'

paradigm [1], aiming to develop a DNN-based surrogate model that captures the constitutive relations embedded in DSMC data.

Garg *et al.* [1] proposed a computationally efficient method (called FVM-DSMC-ML solver). It utilizes *the DSMC data to build a separate database for constitutive relations (CR) guided by NCCRs in advance, instead of using the numerical solutions of higher-order constitutive relations in conventional algebraic or differential forms, and then later combines it with the conservation laws (CL), which are fundamental laws of physics*. The origin of this novel methodology can be traced back to the foundational work in Myong's 1999 article in the *Physics of Fluids*, where the author articulated that "*if a method in which the constitutive relations are stored as a separate database is adopted, the additional computational cost can be trivial compared with the Navier–Stokes relations."* (Ref. 53, p. 2800).

The FVM-DSMC-ML framework presented in [1] is currently only valid for monoatomic gas. In this study, we aim to extend the FVM-DSMC-ML framework to diatomic gases with rotational and vibrational modes by employing the two-temperature framework (translational and rotational) as well as the three-temperature framework (translational, rotational, and vibrational), coupled with deep neural network (DNN)-based DSMC constitutive relations for the viscous stresses and heat fluxes associated with translational, rotational, and vibrational modes.

There are some non-trivial issues in extending the FVM-DSMC-ML solver to diatomic gases. First, it is important to describe rotational and vibrational modes, as there are different ways to handle them. In this study, we use a multi-temperature framework, where each mode has its own temperature, as it is necessary to describe them in the same way as DSMC. Second, developing a successful DNN model for diatomic gases, which have two additional modes (and dimensions on topology) compared to monatomic gases, requires the careful selection of input and output parameters, as well as meticulous attention to the details of various additional parameters such as the number of hidden layers, neurons per layer, epochs, learning rate, etc. In this regard, insights and guidance gained from the theoretical study of NCCRs of diatomic gases are vital to developing compact DNN models for diatomic gases.

As with the monatomic gas case, we will evaluate the performance (computational accuracy and cost) of the new FVM-DSMC-ML solver for diatomic gas for the one-dimensional compressive shock structure problem. The choice of this flow problem is based on its simplicity and relevance for gases in high non-equilibrium states. Shock structures have a significant impact on the overall flow pattern around hypersonic aerospace vehicles flying at high altitudes. It is also well known that stiff shock structures are one of the most difficult problems to solve theoretically and numerically because the physical properties change rapidly over thin regions, in the order of microns, due to extreme self-steeping nonlinearities.

Section II explains in detail the set of physical conservation laws considered for the current study, alongside the formulation utilized to develop DNN-based constitutive relations for diatomic gases. Section III presents the validation studies carried out to test the efficacy of the new FVM-DSMC-ML framework for diatomic gases. In Sec. IV, we construct the topology of the DSMC constitutive relations for diatomic gases (in the compression regime of flow topology), which allows us to understand how a DSMC topology deviates from the NSF topology when the flow is away from local thermal equilibrium.

II. PHYSICAL CONSERVATION LAWS AND CONSTITUTIVE RELATIONS IN MULTI-TEMPERATURE FORMULATION

In most existing works on diatomic gases, the set of conservation laws used by conventional CFD methods is the two-temperature model introduced by Park [5, 63]. This model assumes that the translational and rotational energy modes are in equilibrium, since a comparatively small number of collisions are required to attain equilibrium between the translational and rotational modes, compared to the vibrational modes. Thus, in addition to the conservation of mass momentum and energy, another conservation law is required to account for the changes in the vibrational temperature [64]. Olejniczak & Candler [65] devised a source term in the vibrational energy conservation law to account for the non-equilibrium between the trans-rotational and vibrational energy modes by employing coupling models in the Landau-Teller equation [66]. In the works by Sharma & Gillespie [67] and Kim [68], it was observed that at high temperatures, a non-equilibrium exists between the translational and rotational modes of energy, thus requiring a separate conservation law for the rotational energy.

In the current study, instead of using the conventional two-temperature model [5, 63, 65], we will develop an FVM-DSMC-ML solver for the following three-temperature model of conservation laws,

$$\frac{\partial}{\partial t}\underbrace{\begin{bmatrix}\rho\\ \rho\mathbf{u}\\ \rho E_{tot}\\ \rho E_{rt}\\ \rho E_{vb}\end{bmatrix}}_{\substack{Conserved\\ Variable}} + \nabla\cdot\underbrace{\begin{bmatrix}\rho\mathbf{u}\\ \rho\mathbf{u}\mathbf{u}+p\mathbf{I}\\ (\rho E_{tot}+p)\mathbf{u}\\ \rho E_{rt}\mathbf{u}\\ \rho E_{vb}\mathbf{u}\end{bmatrix}}_{\substack{Inviscid\\ Flux}} + \nabla\cdot\underbrace{\begin{bmatrix}0\\ \boldsymbol{\Pi}\\ \boldsymbol{\Pi}\cdot\mathbf{u}+\mathbf{Q}_{tr}+\mathbf{Q}_{rt}+\mathbf{Q}_{vb}\\ \mathbf{Q}_{rt}\\ \mathbf{Q}_{vb}\end{bmatrix}}_{\substack{Viscous\\ Flux}} + \underbrace{\begin{bmatrix}0\\ 0\\ 0\\ \rho S_{rt}\\ \rho S_{vb}\end{bmatrix}}_{Source} = 0. \tag{2}$$

Here, ρ is the density, $\mathbf{u}$ is the fluid velocity, p is the pressure, and E_{tot} is the total energy. The following relations of the equation of state (EOS), specific heat ratio (γ), and E_{tot} are also assumed (T_{tr}, T_{rt}, T_{vb}, E_{tr}, E_{rt}, E_{vb}, θ_{vb}, T_{DOF}, R_{DOF}, V_{DOF} and R_g are the translational temperature, rotational temperature, vibrational temperature, translational energy, rotational energy, vibrational energy, characteristic vibrational temperature, translational degrees of freedom, rotational degrees of freedom, vibrational degrees of freedom, and gas constant, respectively),

$$\begin{aligned}
&p=\rho R_g T_{tr}, \quad E_{tot}=\frac{1}{2}\mathbf{u}\cdot\mathbf{u}+E_{tr}+E_{rt}+E_{vb},\\
&E_{tr}(T)=\frac{T_{DOF}}{2}R_g T,\\
&E_{rt}(T)=\frac{R_{DOF}}{2}R_g T, \quad E_{vb}(T)=\frac{R_g\theta_{vb}}{\exp\left(\frac{\theta_{vb}}{T}\right)-1},\\
&\gamma=\frac{T_{DOF}+R_{DOF}+V_{DOF}+2}{T_{DOF}+R_{DOF}+V_{DOF}}, \quad V_{DOF}=\frac{2E_{vb}(T_{vb})}{R_g T_{vb}}.
\end{aligned} \tag{3}$$

At this juncture, it is crucial to note that the DSMC solutions satisfy the ideal equation of state (EOS) [16]. The source terms (S_{rt} and S_{vb}) in equation (2) can be defined as follows [60, 64, 65, 69],

$$\begin{aligned}
&S_{rt}=\frac{E_{rt}(T_{tr})-E_{rt}(T_{rt})}{\tau_{rt}}, \quad S_{vb}=\frac{E_{vb}(T_{tr})-E_{vb}(T_{vb})}{\tau_{vb}},\\
&\tau_{rt}=Z_{R-T}\tau_c, \quad \tau_{vb}=Z_{V-T}\tau_c.
\end{aligned} \tag{4}$$

Here, τ_{rt} is the rotational relaxation time, τ_{vb} is the vibrational relaxation time, Z_{R-T} is the relaxation parameter for the rotational and translational energy exchange, Z_{V-T} is the relaxation parameter for the vibrational and translational energy exchange, and τ_c is the mean collision time based on translational temperature. In equation (4), we have not included the term that accounts for the exchange of energy between the vibrational and rotational energy, which was identified in the works by Park [70] and Kim & Boyd [71, 72]. This decision stems from the procedure followed by DSMC to exchange energy. In DSMC, during collisions, both the rotational and vibrational modes exchange energy individually with the translational mode. In this study, we develop a solution methodology that relies on the DSMC results; therefore, vibrational-rotational energy exchange is not included in the source terms.

Previous researchers [11, 18, 19, 59, 60, 73] have demonstrated that the conservation laws of the density, momentum, and total energy in (2) are an exact consequence of the Boltzmann kinetic equation (1). Only with the introduction of approximations such as the linear Navier-Stokes and Fourier (NSF) constitutive relations for viscous shear stress ($\boldsymbol{\Pi}$) and heat fluxes ($\mathbf{Q}_{tr}$, $\mathbf{Q}_{rt}$, and $\mathbf{Q}_{vb}$) in equation (2), do these equations become approximate, thereby restricting their accuracy to conditions near LTE. These linear NSF constitutive relations are as follows,

$$\begin{aligned}
\boldsymbol{\Pi}_{NSF} &= -2\mu\left[\nabla\mathbf{u}\right]^{(2)}, \\
\mathbf{Q}_{tr,NSF} &= -k_{tr}\nabla T_{tr}, \\
\mathbf{Q}_{rt,NSF} &= -k_{rt}\nabla T_{rt}, \\
\mathbf{Q}_{vb,NSF} &= -k_{vb}\nabla T_{vb}.
\end{aligned} \tag{5}$$

Here, μ is the coefficient of viscosity, k_{tr} is the thermal conductivity for translational mode, k_{rt} is the thermal conductivity for rotational mode, k_{vb} is the thermal conductivity for vibrational mode, and the symbol $\left[\mathbf{A}\right]^{(2)}$ stands for the traceless symmetric part of a tensor $\mathbf{A}$.

For a situation where thermal nonequilibrium is prevalent, the constitutive relations of the four undetermined variables in the set of equations (2), i.e., viscous stress ($\boldsymbol{\Pi}$), total heat flux (

$\mathbf{Q} = \mathbf{Q}_{tr} + \mathbf{Q}_{rt} + \mathbf{Q}_{vb}$), rotational heat flux ($\mathbf{Q}_{rt}$), and vibrational heat flux ($\mathbf{Q}_{vb}$) are derived by first differentiating the statistical definition of the variables in time and then combining them with the Boltzmann kinetic equation [11, 59, 60, 73],

$$\begin{aligned}
&\rho\frac{d(\mathbf{\Pi}/\rho)}{dt} + \nabla\cdot\boldsymbol{\psi}^{(\mathbf{\Pi})} + 2[\mathbf{\Pi}\cdot\nabla\mathbf{u}]^{(2)} + 2p[\nabla\mathbf{u}]^{(2)} = \mathbf{\Lambda}^{(\mathbf{\Pi})},\\
&\rho\frac{d(\mathbf{Q}/\rho)}{dt} + \nabla\cdot\boldsymbol{\psi}^{(\mathbf{Q})} + \boldsymbol{\psi}^{(\mathbf{P})} : \nabla\mathbf{u} + \mathbf{Q}\cdot\nabla\mathbf{u} + \frac{d\mathbf{u}}{dt}\cdot\mathbf{\Pi} + \mathbf{\Pi}\cdot\nabla(C_pT) + p\nabla(C_pT) = \mathbf{\Lambda}^{(\mathbf{Q})},\\
&\rho\frac{d(\mathbf{Q}_{rt}/\rho)}{dt} + \nabla\cdot\boldsymbol{\psi}^{(\mathbf{Q}_{rt})} + \mathbf{Q}_{rt}\cdot\nabla\mathbf{u} + \mathbf{\Pi}\cdot\nabla(C_pT_{rt}) + p\nabla(C_pT_{rt}) = \mathbf{\Lambda}^{(\mathbf{Q}_{rt})},\\
&\rho\frac{d(\mathbf{Q}_{vb}/\rho)}{dt} + \nabla\cdot\boldsymbol{\psi}^{(\mathbf{Q}_{vb})} + \mathbf{Q}_{vb}\cdot\nabla\mathbf{u} + \mathbf{\Pi}\cdot\nabla(C_{p,vb}T_{vb}) + p\nabla(C_{p,vb}T_{vb}) = \mathbf{\Lambda}^{(\mathbf{Q}_{vb})}.
\end{aligned} \tag{6}$$

Here, C_p and $C_{p,vb}$ denote the specific heat capacity at constant pressure and the vibrational specific heat capacity at constant pressure, respectively. The constitutive equations (6), $\boldsymbol{\psi}^{(\mathbf{\Pi},\mathbf{Q},\mathbf{P},\mathbf{Q}_{rt},\mathbf{Q}_{vb})}$ represent the open high-order terms associated with the viscous shear stress, the total heat flux, the stress, the rotational heat flux, and the vibrational heat flux, respectively. $\mathbf{\Lambda}^{(\mathbf{\Pi},\mathbf{Q},\mathbf{Q}_{rt},\mathbf{Q}_{vb})}$ on the right-hand side of the equations (6) accounts for the dissipation in non-conserved quantities, which arises from the collision operator in the kinetic equation. It is worth noting that the constitutive equations (6) are an exact consequence of the modified Boltzmann equation [59, 60] which makes them capable of capturing the complete flow physics if accurate closures for the open higher-order terms $\boldsymbol{\psi}^{(\mathbf{\Pi},\mathbf{Q},\mathbf{P},\mathbf{Q}_{rt},\mathbf{Q}_{vb})}$ and $\mathbf{\Lambda}^{(\mathbf{\Pi},\mathbf{Q},\mathbf{Q}_{rt},\mathbf{Q}_{vb})}$ are provided.

In this study, rather than theoretically deriving the precise closed forms of the open higher-order terms in equations (6), we will utilize a combination of closed-form DSMC solution data and DNN to achieve a compact representation of these constitutive relations. Therefore, as pointed out in [1], the current methodology does not suffer the so-called closure problem. Nonetheless, the insights and guidance gained from the theoretical study of equations (6) have proven to be very useful in constructing compact DNN models that map linear viscous stresses and heat fluxes to higher-order viscous stresses and heat fluxes from DSMC data. The decision to employ a DNN model to develop constitutive relations, rather than simpler approaches such as curve fitting, regression, or least-squares methods, is motivated by the high

degree of non-linearity inherent in the self-steepening shock structure problem. Traditional curve-fitting techniques cannot generalize effectively in this context, compromising the model's robustness, i.e., they do not allow the model to predict solutions for intermediate Mach numbers that were not included in the curve-fitting dataset.

As the first step, we develop a DNN model that encompasses the sum of the effects of all the higher-order terms in (6), leading to the closed non-conserved variables predicted by DSMC solutions of diatomic gases. This DNN model of constitutive relations is equivalent to an iterative solver of (6) that predicts the closed DSMC viscous stresses and heat fluxes with the initial prediction as the first-order viscous stresses and heat fluxes from the same solution space. To implement it directly in the conservation laws, the DNN model can be conceptually expressed as follows:

$$\begin{aligned}
\mathbf{\Pi}_{DSMC\ or\ Higher-order} &= f_{\Pi}\left(\mathbf{\Pi}_{NSF}, \mathbf{Q}_{tr,NSF}, \mathbf{Q}_{rt,NSF}, \mathbf{Q}_{vb,NSF}\right), \\
\mathbf{Q}_{tr,DSMC\ or\ Higher-order} &= f_{\mathrm{Q}_{tr}}\left(\mathbf{\Pi}_{NSF}, \mathbf{Q}_{tr,NSF}, \mathbf{Q}_{rt,NSF}, \mathbf{Q}_{vb,NSF}\right), \\
\mathbf{Q}_{rt,DSMC\ or\ Higher-order} &= f_{\mathrm{Q}_{rt}}\left(\mathbf{\Pi}_{NSF}, \mathbf{Q}_{tr,NSF}, \mathbf{Q}_{rt,NSF}, \mathbf{Q}_{vb,NSF}\right), \\
\mathbf{Q}_{vb,DSMC\ or\ Higher-order} &= f_{\mathrm{Q}_{vb}}\left(\mathbf{\Pi}_{NSF}, \mathbf{Q}_{tr,NSF}, \mathbf{Q}_{rt,NSF}, \mathbf{Q}_{vb,NSF}\right).
\end{aligned} \tag{7}$$

One notable difference between equations (6) and the DNN-based implementation of these relations in equations (7) is that instead of choosing total heat flux, we develop the DNN model containing translational heat flux. This choice stems from our goal to understand the topology of each form of energy, including translational, rotational, and vibrational, compared to their first-order counterparts.

At this point, it must be highlighted that the first-order constitutive relations, such as ($\mathbf{\Pi}_{NSF-DSMC} = -2\mu(T_{DSMC})\left[\nabla \mathbf{u}_{DSMC}\right]^{(2)}$), are *introduced in a bookkeeping role*, to facilitate the efficient construction of the topology of DSMC solutions that can be coupled with the conservation laws (2). Since these first-order non-conserved variables are inherently a part of the closed solutions predicted by DSMC, their introduction does not compromise the integrity of the DSMC constitutive data, ensuring that the final solutions remain uncontaminated in principle.

On the other hand, Mankodi & Myong [60] and Srivastava *et al*. [74] proposed simplified second-order NCCR models that effectively capture the intrinsic nonlinearity and strong coupling inherent in the nonlinear coupled constitutive relations, within the context of the conventional two-temperature framework on translational and vibrational, and translational and rotational energy modes, respectively. Combining these two models yields

$$\begin{aligned}
&\hat{\mathbf{\Pi}} q_{2nd}(c\hat{R}) = \hat{\mathbf{\Pi}}_{NSF} + [\hat{\mathbf{\Pi}} \cdot \nabla \hat{\mathbf{u}}]^{(2)}, \\
&\hat{\mathbf{Q}}_{tr} q_{2nd}(c\hat{R}) = \hat{\mathbf{Q}}_{tr,NSF} + \hat{\mathbf{\Pi}} \cdot \hat{\mathbf{Q}}_{tr,NSF}, \\
&\hat{\mathbf{Q}}_{rt} q_{2nd}(c\hat{R}) = \hat{\mathbf{Q}}_{rt,NSF} + \hat{\mathbf{\Pi}} \cdot \hat{\mathbf{Q}}_{rt,NSF}, \\
&\hat{\mathbf{Q}}_{vb} q_{2nd}(c\hat{R}) = \hat{\mathbf{Q}}_{vb,NSF} + \hat{\mathbf{\Pi}} \cdot \hat{\mathbf{Q}}_{vb,NSF},
\end{aligned} \tag{8}$$

where

$$\begin{aligned}
&q_{2nd}(c\hat{R}) = \frac{\sinh(c\hat{R})}{c\hat{R}}, \\
&\hat{R} = \left[\hat{\mathbf{\Pi}} : \hat{\mathbf{\Pi}} + \hat{\mathbf{Q}}_{tr} \cdot \hat{\mathbf{Q}}_{tr} + \hat{\mathbf{Q}}_{rt} \cdot \hat{\mathbf{Q}}_{rt} + \hat{\mathbf{Q}}_{vb} \cdot \hat{\mathbf{Q}}_{vb} \right]^{1/2}.
\end{aligned} \tag{9}$$

In this expression, c is the coefficient of gas power laws [53]. The following hat (^) quantities have been applied to express the constitutive model in a compact form:

$$\begin{aligned}
&M = \frac{u_r}{\sqrt{\gamma R_g T_r}}, \ \mathrm{Re} = \frac{\rho_r u_r L}{\mu_r}, \ N_\delta = \frac{\gamma M^2}{\mathrm{Re}}, \ \mathrm{Kn} = \sqrt{\frac{\pi}{2\gamma}} \frac{N_\delta}{M}, \\
&\mathrm{Ec}_\varphi = \frac{u_r^2}{C_{p,\varphi_r} T_{\varphi,r}}, \ \mathrm{Pr}_\varphi = \frac{c_{p,\varphi_r} \mu_r}{k_{\varphi,r}}, \ \varepsilon_\varphi = \frac{1}{\mathrm{Ec}_\varphi \mathrm{Pr}_\varphi}, \\
&\hat{\mathbf{\Pi}} \equiv \frac{N_\delta}{p} \mathbf{\Pi}, \ \hat{\mathbf{\Pi}}_{NSF} \equiv \frac{N_\delta (-2\mu [\nabla \mathbf{u}]^{(2)})}{p}, \\
&\hat{\mathbf{Q}}_\varphi \equiv \frac{N_\delta}{p} \frac{\mathbf{Q}_\varphi}{\sqrt{T_\varphi / (2\varepsilon_\varphi)}}, \ \hat{\mathbf{Q}}_{\varphi,NSF} \equiv \frac{N_\delta}{p} \frac{(-k_\varphi \nabla T_\varphi)}{\sqrt{T_\varphi / (2\varepsilon_\varphi)}}.
\end{aligned} \tag{10}$$

Here, the subscript φ denotes internal degrees of freedom (translational, rotational, or vibrational), r represents the reference state, and L denotes the characteristic length. The hat (^) quantities introduced above play a critical role in normalizing the value of the flux of non-conserved variables (viscous stresses and heat fluxes) in the present DNN models.

In the present study, similar to the monatomic gas case, we will focus on the development of DNN-based constitutive relations for the compressive zone of the diatomic gas flows through the one-dimensional shock structure problem. A stationary shock wave structure represents a purely one-dimensional compressive flow of gas that appears as a very thin segment of a stationary gas region (with the scales of the order of mean free path) [75]. It manifests itself between the supersonic flow upstream and the subsonic flow downstream. This flow is the most extensively studied problem in non-equilibrium gas dynamics [52, 76-78], as a full understanding of its physical behavior has significant scientific and technological consequences. Further, this flow provides an advantage in the computational study (i.e., the absence of boundary conditions), making it an ideal test problem to demonstrate the new FVM-DSMC-ML framework (as the solution is devoid of solid wall boundary effects).

The full set of conservation laws in equation (2) can be simplified for the one-dimensional shock structure problem as follows,

$$\frac{\partial}{\partial t}\underbrace{\begin{bmatrix}\rho\\ \rho u\\ \rho E_{tot}\\ \rho E_{rt}\\ \rho E_{vb}\end{bmatrix}}_{\substack{Conserved\\ Variable}} + \frac{\partial}{\partial x}\underbrace{\begin{bmatrix}\rho u\\ \rho u^2+p\\ (\rho E_{tot}+p)u\\ \rho E_{rt}u\\ \rho E_{vb}u\end{bmatrix}}_{\substack{Inviscid\\ Flux}} + \frac{\partial}{\partial x}\underbrace{\begin{bmatrix}0\\ \Pi_{xx}\\ \Pi_{xx}u+\mathrm{Q}_{tr,x}+\mathrm{Q}_{rt,x}+\mathrm{Q}_{vb,x}\\ \mathrm{Q}_{rt,x}\\ \mathrm{Q}_{vb,x}\end{bmatrix}}_{\substack{Viscous\\ Flux}} + \underbrace{\begin{bmatrix}0\\ 0\\ 0\\ \rho S_{rt}\\ \rho S_{vb}\end{bmatrix}}_{Source} = 0. \qquad (11)$$

To underscore the critical role of higher-order constitutive relations, Fig. 1 compares the temperature distributions and essential thermophysical properties, specifically the specific heat ratio and vibrational degrees of freedom, within the shock structure for solutions obtained from NSF and DSMC. The differences in numerical predictions between these solvers arise from their distinct approaches to estimating viscous shear stress and heat fluxes via their respective constitutive relations.

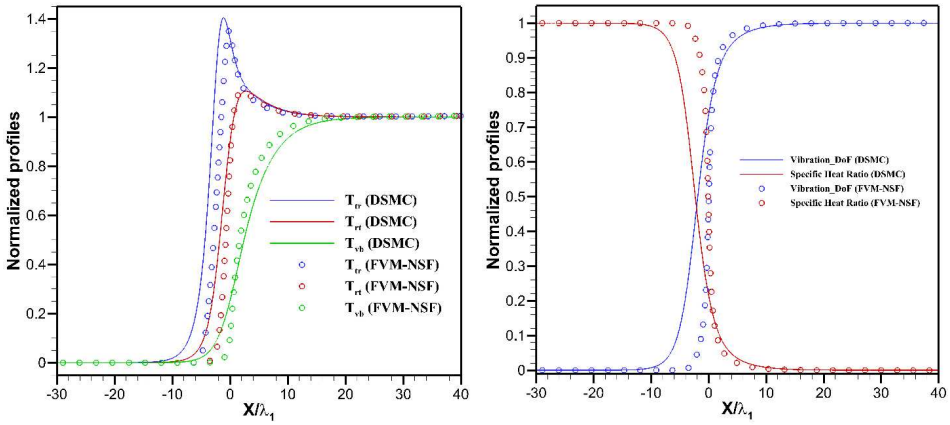

(a) Temperature (b) Thermophysical properties

FIG. 1. Comparison of normalized (a) temperature profiles and (b) key thermophysical properties predicted by NSF and DSMC at a specific Mach number, M = 10 for diatomic gas (nitrogen).

The analysis of shock profiles illustrated in Fig. 1 indicates significant differences in the upstream region between the profiles predicted by the FVM-NSF solver and those obtained from the DSMC solution. They arise from variations in the distribution of non-conserved variables across the shock structure in the two approaches. Figure 2 compares these non-conserved variables computed from both the FVM-NSF and DSMC solvers.

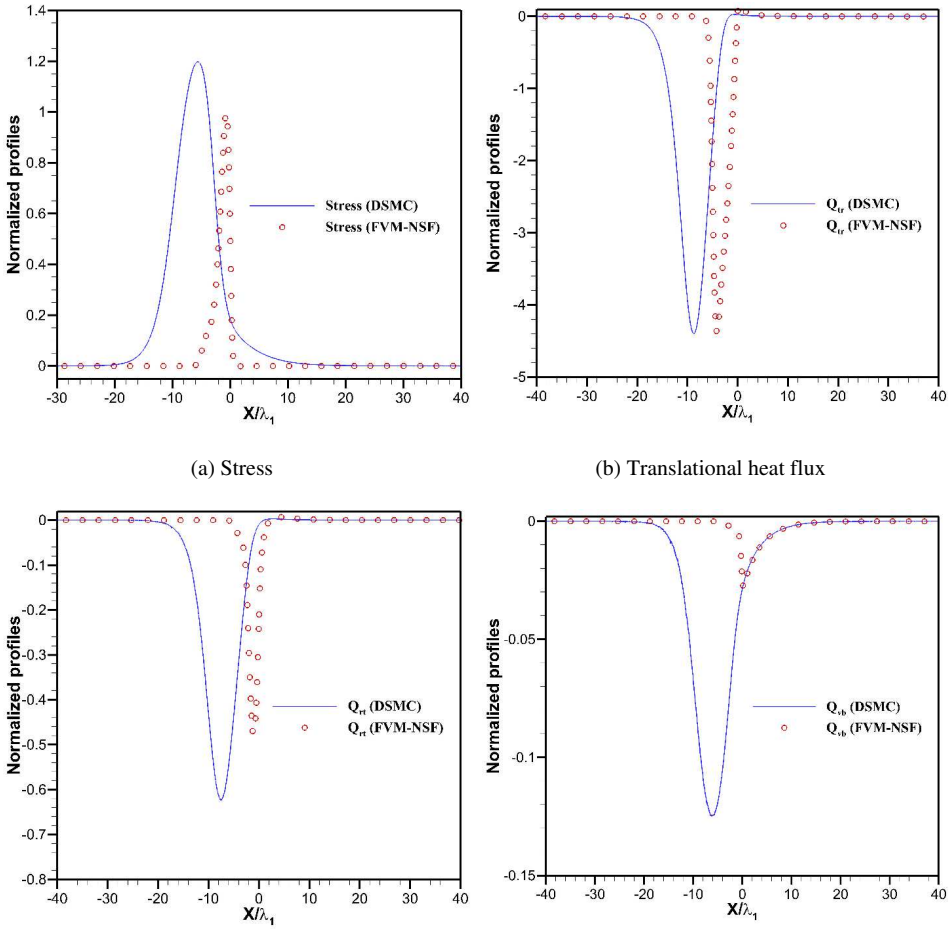

(a) Stress

(b) Translational heat flux

(c) Rotational heat flux

(d) Vibrational heat flux

FIG. 2. Comparison of non-conserved variables across the shock structure (M=10) for diatomic gas (nitrogen): (a) stress, (b) translational heat flux, (c) rotational heat flux, and (d) vibrational heat flux for FVM-NSF and DSMC solvers.

A. Computational methodology

The computational methodology consists of two main components. The first involves the development of a DNN model that incorporates the extracted DSMC (or higher-order constitutive) relationships. The

second component entails the development of a finite volume method (FVM) solver designed to solve the conservation laws in conjunction with the DNN model of constitutive relations. The FVM solver employed in this study is based on a second-order monotonic upwind scheme for conservation laws (MUSCL) [79] with a minmod limiter, alongside the Harten-Lax-van Leer-Contact (HLLC) flux solver [80] for the convective terms and a central difference scheme for the viscous terms. Time integration of the conservation laws is performed using the explicit Euler method.

The specifics of the algorithm utilized to develop the DNN model for DSMC (or the solution methodology incorporating the higher-order constitutive relations) can be summarized as follows:

Step 1. Generation of the DSMC data. In this study, numerical solutions to the flow problem are obtained for a range of critical parameters, specifically Mach numbers in the context of the shock structure problem, using DSMC. This approach yields the solutions for viscous stress and heat fluxes in the DSMC framework (Π_{DSMC}, $Q_{tr,DSMC}$, $Q_{rt,DSMC}$ and $Q_{vb,DSMC}$).

Step 2. Computing the distribution of first-order viscous stresses and heat fluxes employing the values of macroscopic properties predicted by DSMC.

a) NSF linear viscous stress ($\Pi_{NSF(DSMC)}$) – This is computed based on the velocity information acquired in Step 1. The viscosity (μ) in the viscous stress calculation is assumed to be a function of total temperature. The mathematical expression for linear viscous stress is as follows,

$$\Pi_{NSF(DSMC)} = -\frac{4}{3}\mu\frac{du}{dx}, \quad \mu = \mu_{\text{ref}}\left(T/T_{ref}\right)^{\omega}. \tag{12}$$

Here, μ_{ref} is the reference viscosity, T_{ref} the reference temperature, and ω the coefficient of viscosity. In the present work, ω is '0.74' (VHS molecule), μ_{ref} is 1.656 $\times 10^{-5}$ kg/m·s, and T_{ref} is 273.15 K.

b) NSF linear translational heat flux ($Q_{tr,NSF(DSMC)}$) – This is computed based on the translational temperature information acquired in Step 1. The thermal conductivity is calculated using the Eucken's relation [81, 82]. The mathematical expression for linear translational heat flux is as follows,

$$Q_{tr,NSF(DSMC)} = -k_{tr}\frac{dT_{tr}}{dx}, \quad k_{tr} = \frac{5}{2}\mu\left(T_{tr}\right)C_{v,tr}. \tag{13}$$

Here, viscosity (μ) is the function of translational temperature and is computed based on the relation provided in equation (12). The value of specific heat at constant volume ($C_{v,tr}$) is calculated using the relation, $C_{v,tr} = R_g/\left(\gamma - 1\right)$ where the value of specific heat (γ) is computed using the relation provided in equation (3).

c) NSF linear rotational heat flux ($Q_{rt,NSF(DSMC)}$) – This is computed based on the rotational temperature information acquired in Step 1. The thermal conductivity is calculated using Eucken's relation [81, 82]. Similar to translational heat flux, it can be mathematically expressed as follows,

$$Q_{rt,NSF(\mathrm{DSMC})} = -k_{rt}\frac{dT_{rt}}{dx}, \quad k_{rt} = \mu\left(T_{rt}\right)C_{v,rt}. \tag{14}$$

Here, viscosity (μ) is the function of rotational temperature and is computed based on the power-law formulation provided in equation (12). The specific heat at constant volume ($C_{v,rt}$) is calculated using the same formulation as for $C_{v,tr}$.

d) NSF linear vibrational heat flux ($Q_{vb,NSF(DSMC)}$) – This is computed based on the vibrational temperature information acquired in Step 1. The thermal conductivity is calculated using the relationship provided by Casseau [82]. It can be mathematically expressed as follows,

$$\mathrm{Q}_{vb,NSF(\mathrm{DSMC})} = -k_{vb}\frac{dT_{vb}}{dx}, \quad k_{vb} = 1.2\mu\left(T_{vb}\right)C_{v,vb}, \quad C_{v,vb} = \frac{R_g\left(\frac{\theta_{vb}}{T_{vb}}\right)^2 \exp\left(\frac{\theta_{vb}}{T_{vb}}\right)}{\left(\exp\left(\frac{\theta_{vb}}{T_{vb}}\right)-1\right)^2} \tag{15}$$

Here, viscosity (μ) is the function of vibrational temperature and is computed based on the power-law formulation provided in equation (12).

Step 3. The DNN model for constitutive relations is trained using $\Pi_{NSF(DSMC)}$ (as described in Step 2a), $\mathrm{Q}_{tr,NSF(DSMC)}$ (as detailed in Step 2b), $\mathrm{Q}_{rt,NSF(DSMC)}$ (as detailed in Step 2c), and $\mathrm{Q}_{vb,NSF(DSMC)}$ (as detailed in Step 2d) as inputs, with outputs represented by Π_{DSMC}, $\mathrm{Q}_{tr,DSMC}$, $\mathrm{Q}_{rt,DSMC}$, and $\mathrm{Q}_{vb,DSMC}$ or the equivalent higher-order values. This model maps the linear viscous stress and heat fluxes to their DSMC or higher-order counterparts.

Figure 3 shows a conceptual diagram of the DNN model of constitutive relations for the multi-temperature framework. Developing a successful DNN model requires the careful selection of input and output parameters, as well as meticulous attention to the details of various additional parameters. These include the number of hidden layers, neurons per layer, epochs, learning rate, batch size, activation functions, regularization techniques, and optimization functions. In this study, the '**Adam**' optimizer [83] was chosen, along with a combination of '**ELU**' [84], '**Leaky-ReLU**' [85], and '**Mish**' [86] activation functions for training the DNN model of constitutive relations. To prevent overfitting, a blend of L1 and L2 regularization was applied. The numeric values for these parameters, influenced by data quality and dataset size, were tailored specifically to address the problem and reduce overfitting risks.

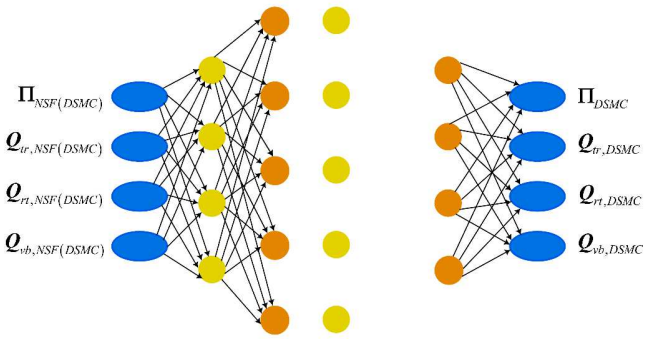

FIG. 3. Conceptual representation of the DNN model of constitutive relations for the multi-temperature framework when both rotational and vibrational degrees of freedom are active.

The next phase entails embedding the DNN model into a standard FVM framework, which is systematically achieved using the following algorithm:

Step I. The NSF flux at the cell interface is calculated using the methodology detailed in Step 2. In this procedure, the macroscopic properties used for calculation are the initial values corresponding to the current iteration.

Step II. The value of the NSF flux is normalized using the methodology thoroughly described by Mankodi & Myong [60] and Srivastava *et al*. [74] and given in (10). These normalized values serve as the input for the DNN model, while the corrected flux, i.e., the output from the DNN model, is relayed back to the FVM solver.

Step III. The solution for the current iteration proceeds by using these corrected fluxes provided by the DNN model.

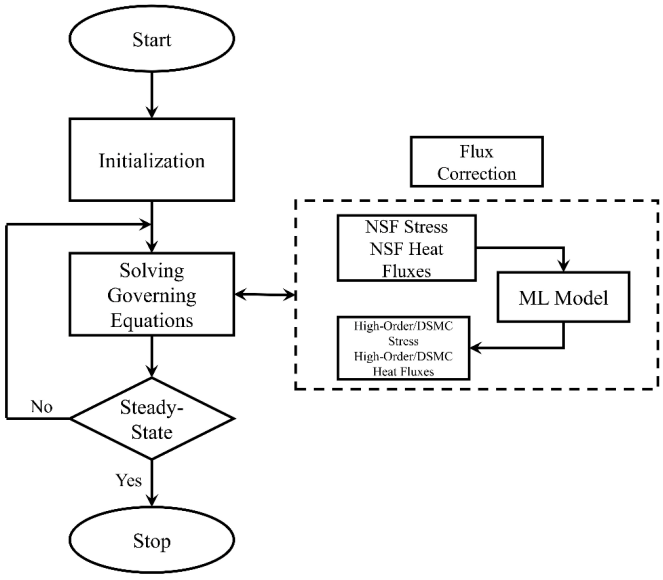

FIG. 4. Flowchart of the algorithm implemented in the FVM-DSMC-ML solver.

The FVM-ML solver continues to iterate until convergence is reached. The progress of the simulation toward convergence is tracked by calculating the L1 error in the macroscopic properties defined as

$$\text{L1 } error = \frac{1}{N_{cell}} \sum_{i=1}^{N_{cell}} abs\left(\phi_i^{t+1} - \phi_i^t\right). \tag{16}$$

In this equation, ϕ represents the translational, rotational, and vibrational temperatures, while N_{cell} refers to the mesh count. The solution is assumed to reach convergence when the L1 error value is below 10^{-4} for all monitored macroscopic properties. Figure 4 illustrates the flow chart of the algorithm implemented in the FVM-DSMC-ML solver.

III. DSMC SOLUTIONS USING THE FVM-DSMC-ML SOLVER FOR DIATOMIC GASES

This section describes the validation studies of the FVM-DSMC-ML framework developed for diatomic gases. In the first case, a DNN model of constitutive relations is developed for diatomic gases in

which only the rotational degrees of freedom are active. In the second case, another DNN model is developed for diatomic gases, where not only rotational degrees of freedom but also vibrational degrees of freedom are activated. In both cases, we develop a single DNN model that can cover full flow regimes across all Mach numbers.

A. Validation of the two-temperature framework

Before evaluating the performance of the FVM-DSMC-ML solver for the full three-temperature framework given in equation (2), we consider a simpler case in which only one additional internal degree of freedom—the rotational degree of freedom—is activated. The corresponding set of conservation laws for the one-dimensional shock structure problem is as follows:

$$\frac{\partial}{\partial t}\begin{bmatrix}\rho\\ \rho u\\ \rho E_{tot}\\ \rho E_{rt}\end{bmatrix}+\frac{\partial}{\partial x}\begin{bmatrix}\rho u\\ \rho u^2+p\\ (\rho E_{tot}+p)u\\ \rho E_{rt}u\end{bmatrix}+\frac{\partial}{\partial x}\begin{bmatrix}0\\ \Pi_{xx}\\ \Pi_{xx}u+\mathrm{Q}_{tr,x}+\mathrm{Q}_{rt,x}\\ \mathrm{Q}_{rt,x}\end{bmatrix}+\begin{bmatrix}0\\ 0\\ 0\\ \rho S_{rt}\end{bmatrix}=0. \tag{17}$$

By applying the strategy described in Sec. II, the non-conserved variables (Π, Q_{tr}, Q_{rt}) appearing in the conservation laws (17) will be determined using the following DNN-based DSMC constitutive relations,

$$\begin{aligned}\Pi_{DSMC}&=f_{\Pi}\left(\Pi_{NSF},\mathrm{Q}_{tr,NSF},\mathrm{Q}_{rt,NSF}\right),\\ \mathrm{Q}_{tr,DSMC}&=f_{\mathrm{Q}_{tr}}\left(\Pi_{NSF},\mathrm{Q}_{tr,NSF},\mathrm{Q}_{rt,NSF}\right),\\ \mathrm{Q}_{rt,DSMC}&=f_{\mathrm{Q}_{rt}}\left(\Pi_{NSF},\mathrm{Q}_{tr,NSF},\mathrm{Q}_{rt,NSF}\right).\end{aligned} \tag{18}$$

Figure 5 shows a conceptual diagram of the DNN model of constitutive relations for the multi-temperature framework when only rotational degrees of freedom are active. The computational methodology for this simpler case exactly follows the approach outlined in Sec. II A, with the sole adjustment being the omission of steps related to vibrational degrees of freedom.

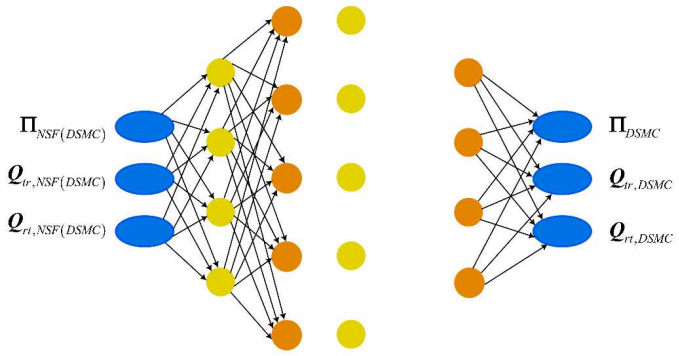

FIG. 5. Conceptual representation of the DNN model of constitutive relations for the multi-temperature framework when only rotational degrees of freedom are active.

The DSMC simulations are carried out with a diatomic gas (nitrogen with a molecular diameter of 4.17 $\times 10^{-10}$ m and molecular mass of 4.64885×10^{-26} kg). For all simulations, the viscosity index (ω) is set to 0.74, assuming a variable hard sphere (VHS) model. The upstream pressure (p_1), temperature (T_1), and specific heat ratio (γ) are 6.0651 Pa, 300 K, and 1.4, respectively. The mean free path in the upstream region (λ_1) is 8.8396×10^{-4} m, with a computational cell width equal to 1/50th of this mean free path. The time step for the DSMC simulations is 1/100th of the mean collision time (τ_c) based on the upstream conditions. The rotational degrees of freedom (R_{DOF}) and rotational relaxation parameter (Z_{R-T}) are 2 and 5 [87], respectively. The weight ratio, defined as the number of real molecules per DSMC particle, is 5.0×10^{13}, and the simulation domain spans from [−250.0, 250.0] times the upstream mean free path. Using these upstream conditions and the flow Mach number (M_1), the remaining downstream macroscopic properties are determined based on the Rankine–Hugoniot relations, as summarized below,

$$\frac{p_2}{p_1} = 1 + \frac{2\gamma}{\gamma+1}\left(M_1^2 - 1\right),$$
$$M_2^2 = \frac{1 + \left[(\gamma-1)/2\right]M_1^2}{\gamma M_1^2 - (\gamma-1)/2}, \tag{19}$$
$$\frac{T_2}{T_1} = \left[1 + \frac{2\gamma}{(\gamma+1)}\left(M_1^2 - 1\right)\right]\left[\frac{2 + (\gamma-1)M_1^2}{(\gamma+1)M_1^2}\right].$$

In the equations above, subscript '1' denotes the upstream conditions, while subscript '2' denotes the downstream conditions. The initial discontinuity is located at the center of the computational domain. Data for developing the DNN model is generated using an in-house MPI parallelized DSMC solver.

In the present in-house DSMC solver, sampling cells are intentionally configured to match the collision cells, providing the enhanced resolution essential for accurate DNN modeling. The DSMC solution performs sampling until the viscous stress (Π_{DSMC}), translational heat flux ($Q_{tr,DSMC}$), and rotational heat flux ($Q_{rt,DSMC}$) values stabilize, typically requiring approximately 0.2 million samples. Despite this extensive sampling, the calculated values for linear viscous stress ($\Pi_{NSF(DSMC)}$), linear translational heat flux ($Q_{tr,NSF(DSMC)}$), and linear rotational heat flux ($Q_{rt,NSF(DSMC)}$) remain noisy due to the probabilistic nature of the DSMC. To obtain a smooth solution for the linear viscous stress ($\Pi_{NSF(DSMC)}$) and heat fluxes ($Q_{tr,NSF(DSMC)}$ and $Q_{rt,NSF(DSMC)}$), after sampling these values (detailed in Sec. II A) are filtered. The algorithm applied to achieve the filtered solution can be summarized as follows:

1) The values of linear viscous stress and heat flux are treated as spatially dependent signals. The first step involves computing the fast Fourier transform (FFT) of these signals, yielding a frequency-amplitude distribution. This distribution identifies the cutoff frequency, defined as the frequency beyond which the amplitudes of linear viscous stress, linear translational heat flux, and linear rotational heat flux become negligible.

2) In the subsequent step, the data is filtered using a low-pass filter based on this frequency. In the present study, a second-order Butterworth filter is employed.

The DNN model of the DSMC constitutive relations is trained using filtered linear viscous stress and heat flux data as inputs, with corresponding DSMC viscous stress and heat flux data as outputs. For practical applications, the DNN model of constitutive relations should reliably predict accurate non-conserved variables across a broad range of Mach numbers. For this purpose, a single DNN model is developed using DSMC data for Mach numbers 2, 3, 4, 5, 6, 7, 8, 9, and 10. Shock structure simulations are subsequently conducted using the FVM-DSMC-ML solver (see Sec. II A), and the results are validated against actual DSMC solutions to evaluate its performance under two conditions: (1) for Mach numbers that were included in the DNN model's training dataset, and (2) for intermediate Mach numbers, specifically 2.5, 4.5, 6.5, and 8.5, which were not part of the training data.

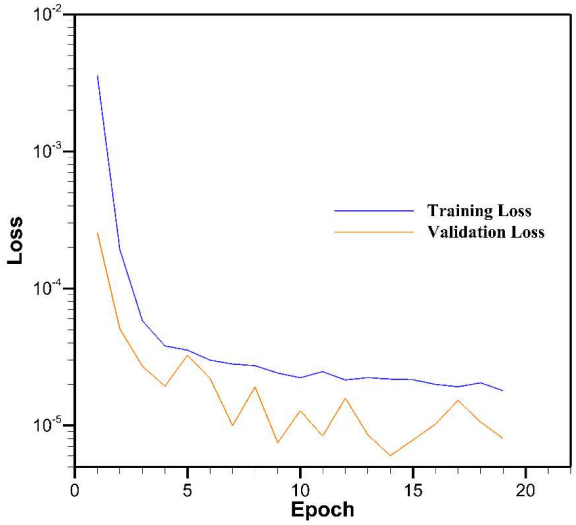

FIG. 6. Progress of root mean square loss for training and validation in the DNN modeling (two-temperature framework).

Figure 6 illustrates the evolution of the root mean square (RMS) loss for both the training and validation datasets as the DNN model is progressively trained within the two-temperature framework. The key hyperparameters employed for model training are summarized in Table I. Notably, the number of training epochs is not explicitly specified in the table, as it was determined dynamically based on an early stopping criterion with a patience parameter set to '5'.

TABLE I. Summary of hyperparameters employed in training the DNN model for multi-temperature constitutive relation.

Hyperparameter	Two-temperature framework	Three-temperature framework
Number of hidden layers	4	4
Activation function	[LeakyReLU, ELU, ELU, LeakyReLU]	[Mish, ELU, ELU, LeakyReLU]
Number of neurons	[16, 16, 16, 15]	[14, 14, 14, 13]
Optimizer	Adam	Adam
Learning rate	0.0003	0.0003
Batch	25	25
L1 regularization	0.2e-6	0.2e-6
L2 regularization	0.2e-6	0.2e-6

Lumpkin & Boyd [88] proposed that when comparing particle-based solutions (such as DSMC) with continuum-based solutions (like the FVM method), the rotational relaxation parameter term for the continuum approach ($Z_{R\text{-}T,CFD}$) should be higher than that for the particle-based approach ($Z_{R\text{-}T,DSMC}$), i.e., $Z_{R\text{-}T,CFD} \geq 2Z_{R\text{-}T,DSMC}$. This difference arises because of the different implementations of rotational energy exchange. The DSMC method employs the collision model by Larsen and Borgnakke [22], which assumes that a specific fraction of collisions ($\chi_{in-elastic} = 1/Z_{R-T,DSMC}$) results in thermal relaxation by allowing the exchange of translational energy with an internal energy mode. In contrast, the continuum method employs the Jeans equation (4) [69] where the relaxation is defined as $Z_{R-T,continuum} = \tau_{rt}/\tau_c$.

In this study, we determine the rotational relaxation parameter value for the FVM-DSMC-ML solver based on the relationship $Z_{R\text{-}T,FVM\text{-}DSMC\text{-}ML} = 1.2Z_{R\text{-}T,DSMC}$ such that the viscous stress and heat fluxes of

the FVM-DSMC-ML solver may align closely with those in the DSMC solution. Since these viscous stress and heat flux results from the particle-based method with internal energy exchange intrinsic to DSMC, the FVM-DSMC-ML solver exhibits source relaxation behavior similar to that of DSMC. Consequently, the Jeans source term in equation (17), which governs energy exchange between the translational and rotational energy modes [69], requires a relaxation parameter closer to the one used in DSMC.

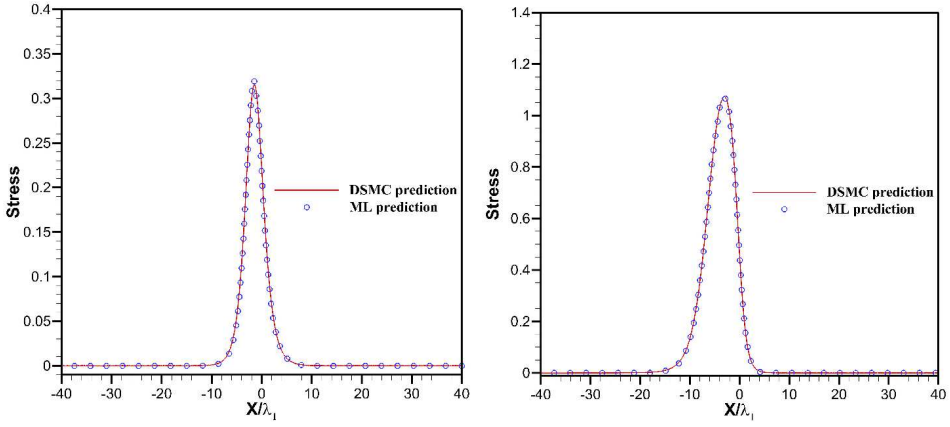

(a) M = 2 (b) M = 8.5

FIG. 7. Comparison of viscous stress profiles predicted by the DNN model of DSMC constitutive relations for the two-temperature framework, developed using the DSMC data of Mach numbers 2, 3, 4, 5, 6, 7, 8, 9, and 10, with the actual DSMC results for Mach numbers: (a) 2 and (b) 8.5.

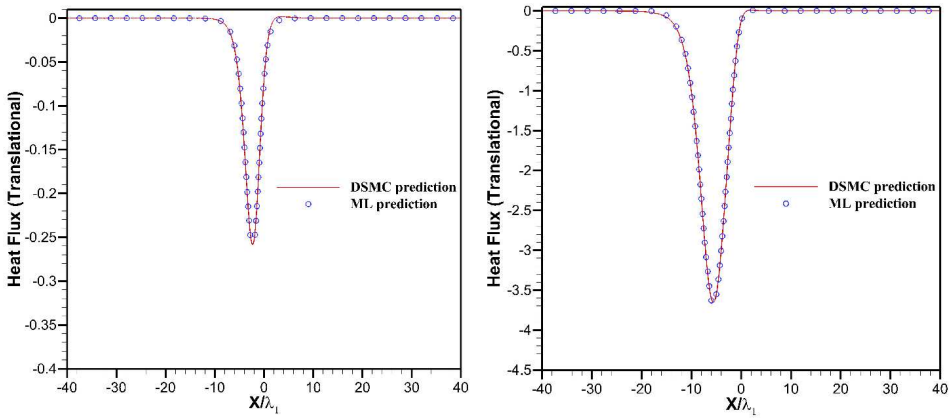

(a) M = 2 (b) M = 8.5

FIG. 8. Comparison of translational heat flux profiles predicted by the DNN model of constitutive relations for the two-temperature framework, developed using the DSMC data for Mach numbers 2, 3, 4, 5, 6, 7, 8, 9, and 10, with the actual DSMC results for Mach numbers: (a) 2 and (b) 8.5.

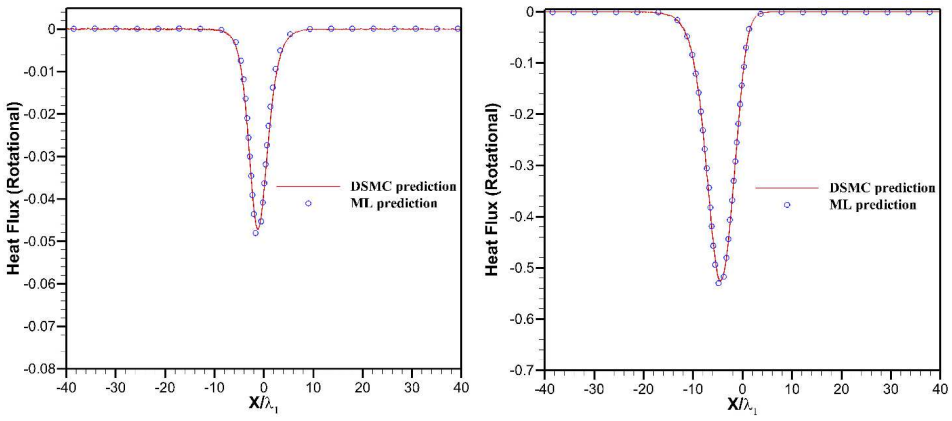

(a) M = 2 (b) M = 8.5

FIG. 9. Comparison of rotational heat flux profiles predicted by the DNN model for constitutive relations in the two-temperature framework, developed using the DSMC data for Mach numbers 2, 3, 4, 5, 6, 7, 8, 9, and 10, with the actual DSMC results for Mach numbers: (a) 2 and (b) 8.5.

Before performing FVM-DSMC-ML simulations of conserved (density, velocity, and all temperatures) and non-conserved (viscous stress and all heat fluxes) properties, we compare non-conserved properties estimated by the DNN model with the actual DSMC results. For brevity, Figs. 7, 8, and 9 present comparisons of viscous stress, translational heat flux, and rotational heat flux for Mach numbers 2 and 8.5, respectively. These figures demonstrate that the DNN model provides results in close agreement with those obtained from the DSMC simulations.

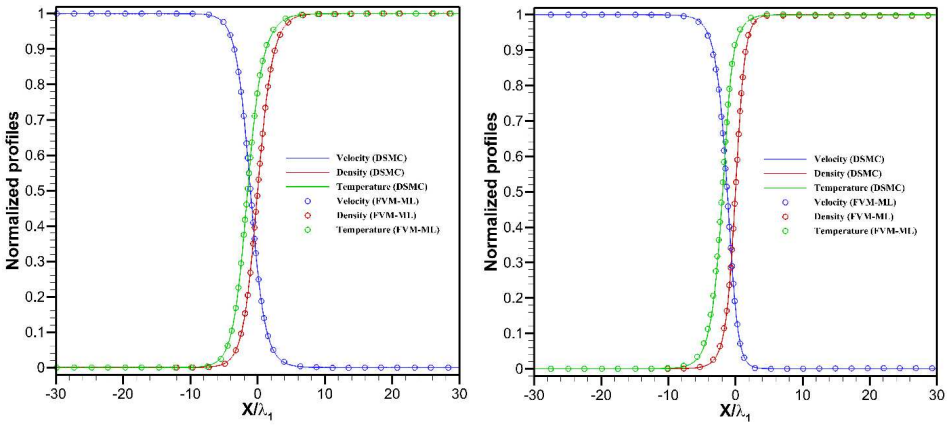

(a) M = 2 (b) M = 4.5

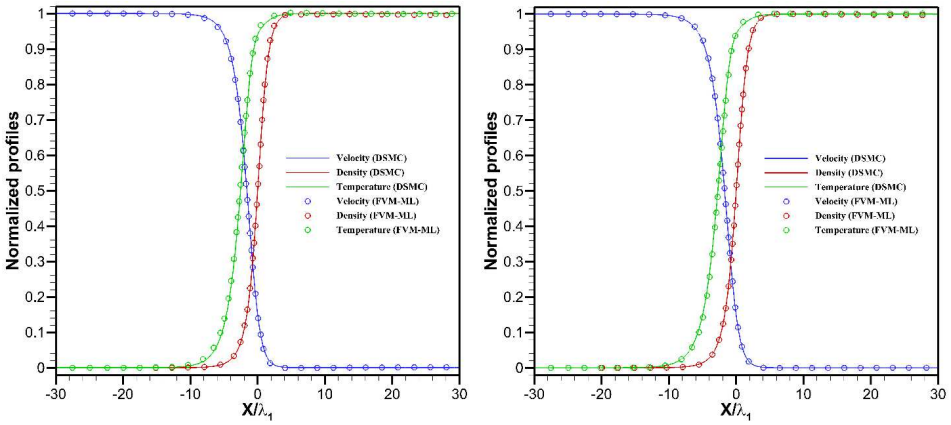

(c) M = 8.5 (d) M = 10

FIG. 10. Comparison of normalized conserved properties (density, velocity, and total temperature) of the FVM-DSMC-ML (two-temperature) and DSMC solutions for Mach numbers: (a) 2, (b) 4.5, (c) 8.5, and (d) 10. The DNN model here is trained using DSMC data from Mach numbers 2, 3, 4, 5, 6, 7, 8, 9, and 10.

Figure 10 compares the normalized conserved properties of the FVM-DSMC-ML (two-temperature) and DSMC solutions for Mach numbers 2, 4.5, 8.5, and 10. The DNN model is trained using DSMC data from Mach numbers 2, 3, 4, 5, 6, 7, 8, 9, and 10. The conserved macroscopic properties are normalized employing the following relation:

$$\Phi_{norm} = \frac{\Phi_{cell} - \Phi_1}{\Phi_2 - \Phi_1}, \text{ where } \Phi \text{ is either } \rho \text{ or } T, \tag{20}$$

$$V_{norm} = \frac{V_{cell} - V_2}{V_1 - V_2}. \tag{21}$$

The FVM-DSMC-ML results for all the cases show excellent agreement with DSMC solutions.

Figure 11 compares translational and rotational temperatures of the FVM-DSMC-ML (two-temperature) and DSMC solutions for Mach numbers 2, 4.5, 8.5, and 10. It shows that the FVM-DSMC-ML solver results in close agreement with those produced by the DSMC method.

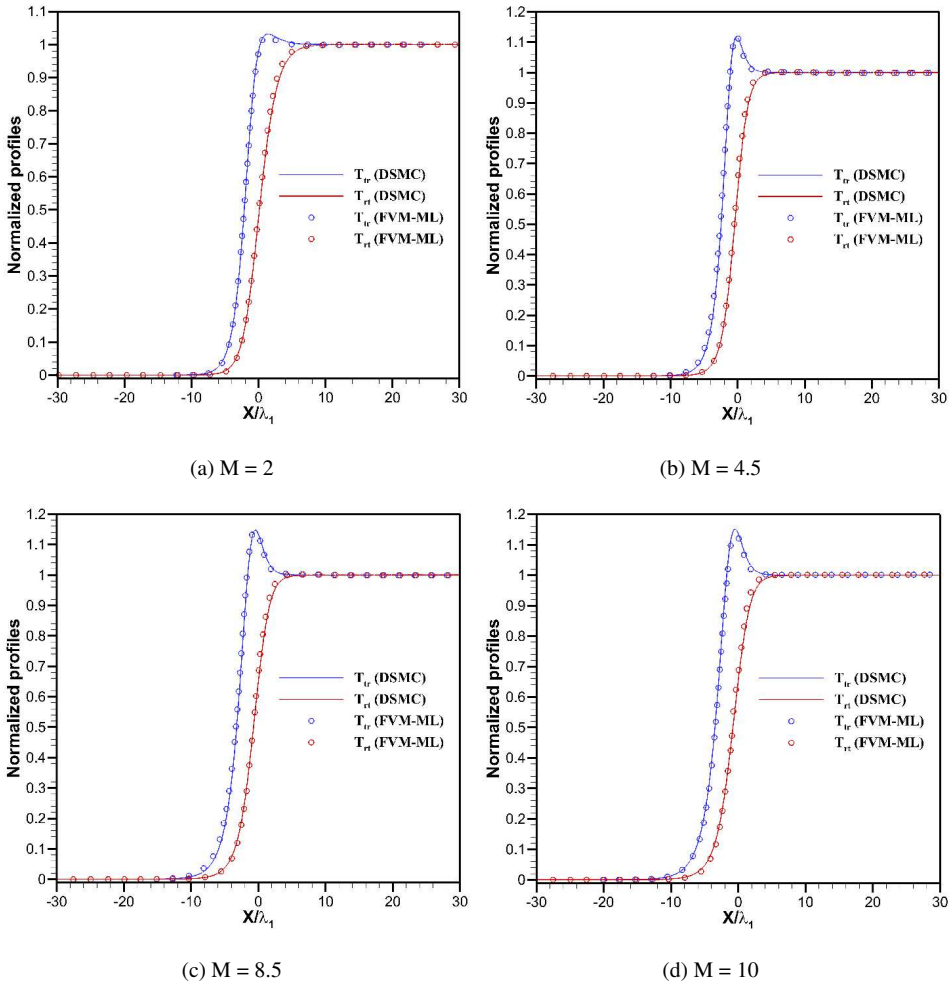

(a) M = 2 (b) M = 4.5

(c) M = 8.5 (d) M = 10

FIG. 11. Comparison of normalized conserved properties (translational and rotational temperatures) of the FVM-DSMC-ML (two-temperature) and DSMC solutions for Mach numbers: (a) 2, (b) 4.5, (c) 8.5, and

(d) 10. The DNN model here is trained using DSMC data from Mach numbers 2, 3, 4, 5, 6, 7, 8, 9, and 10.

In terms of computational cost, the FVM-DSMC-ML solver demonstrates a slight increase, ranging from 1.2 to 1.3 times that of the FVM-NSF solver, with the maximum value of 1.3 observed at a high Mach number of 10. However, when compared to the DSMC solver, the FVM-DSMC-ML solver achieves a drastic reduction in computational time, requiring only 1/20 of the time taken by the conventional DSMC solver. Excluding the cost associated with training DSMC data generation, the computational expense of training the machine learning model constitutes a one-time investment, as the objective is to develop an *a priori portable* model. This training cost is approximately $1/15^{th}$ of the computational effort required to simulate a 1D high Mach number shock structure using an FVM-NSF solver.

B. Validation of the three-temperature framework

We now evaluate the performance of the FVM-DSMC-ML solver for the full three-temperature framework given in equations (2) and (11). Nitrogen is again used as the working gas. The DSMC data for this case is produced using an in-house DSMC solver with MPI parallelization (where sampling cells are the same as collision cells). The upstream pressure (p_1) and temperature (T_1) are set to 10.0563 Pa and 1000 K, respectively. The weight ratio, indicating the number of real molecules per DSMC particle, is 3.8×10^{13}, and the simulation domain extends from [−250.0, 250.0] times the upstream mean free path. The vibrational relaxation parameter (Z_{V-T}) is assigned a value of 50 and the vibrational degrees of freedom (V_{DOF}) is set to 1. Based on upstream pressure and temperature, the mean free path (λ_1) is calculated as 1.7771×10^{-3} m. All other parameters are the same as those specified in Sec. III A.

The excitation of vibrational degrees of freedom results in a shock structure problem characterized by a varying specific heat ratio (γ) across the two sides of the diaphragm. Given a set of pre-shock (upstream) conditions, the post-shock (downstream) conditions can be analytically derived using the

following generalized Rankine–Hugoniot shock relations [60, 89, 90], which account for the impact of the variable specific heat ratio,

$$\begin{aligned}
&\frac{p_2}{p_1} = \frac{1+\gamma_1 M_1^2}{1+\gamma_2 M_2^2}, \\
&\frac{\left(1+\gamma_2 M_2^2\right)^2}{\left(\frac{\gamma_2}{\gamma_2-1}+\frac{\gamma_2}{2}M_2^2\right)\gamma_2 M_2^2} = \frac{\left(1+\gamma_1 M_1^2\right)^2}{\left(\frac{\gamma_1}{\gamma_1-1}+\frac{\gamma_1}{2}M_1^2\right)\gamma_1 M_1^2}, \\
&\frac{u_2}{u_1} = \sqrt{\frac{\gamma_2}{\gamma_1}}\frac{M_2}{M_1}\sqrt{\frac{\frac{\gamma_1}{\gamma_1-1}+\frac{\gamma_1}{2}M_1^2}{\frac{\gamma_2}{\gamma_2-1}+\frac{\gamma_2}{2}M_2^2}}, \\
&\frac{T_2}{T_1} = \frac{\frac{\gamma_1}{\gamma_1-1}+\frac{\gamma_1}{2}M_1^2}{\frac{\gamma_2}{\gamma_2-1}+\frac{\gamma_2}{2}M_2^2}.
\end{aligned} \tag{22}$$

Here, subscripts '1' and '2' represent the upstream and downstream states, respectively. The relationship between the specific heat ratio and internal degrees of freedom is given in equation (3). Notably, for a given upstream Mach number, the downstream specific heat ratio depends on the post-shock temperature, thereby forming an implicit system. Determining the post-shock conditions thus requires an iterative numerical procedure based on the generalized Rankine–Hugoniot shock relations. The initial discontinuity is located at the center of the computational domain.

In the DSMC solver, sampling is performed until the macroscopic properties such as viscous stress and heat fluxes stabilize, requiring approximately one million samples. The linear viscous stress and heat flux components (translational, rotational, and vibrational) are filtered based on the algorithm detailed in Sec. III A to ensure smooth distributions. The DNN model of the DSMC constitutive relations is trained using filtered linear viscous stress and heat flux data as inputs, with corresponding DSMC viscous stress and heat flux data as outputs. Similar to the two-temperature case, a single DNN model is developed using DSMC data for Mach numbers 4, 5, 6, 7, 8, 9, and 10.

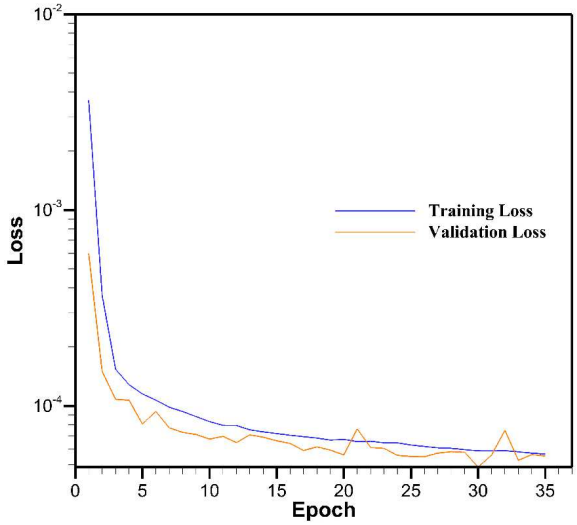

FIG. 12. Progress of root mean square loss for training and validation in the DNN modeling (three-temperature framework).

Similar to the analysis presented in Section III.A, Fig. 12 illustrates the progression of the root mean square loss for both training and validation datasets during the training of the DNN model for the three-temperature framework. The hyperparameters selected for training the DNN model in this case are listed in Table I. An early stopping criterion with a patience of '5' was employed. Following training, neural network-based shock structure simulations are performed using the FVM-DSMC-ML solver (see Sec. II A), and their outcomes are validated against actual DSMC solutions to assess its performance under two scenarios: (1) for Mach numbers present in the DNN model's training dataset, and (2) for intermediate Mach numbers—specifically 4.5, 6.5, and 8.5—that were not included in the training data.

As done in Sec. III A, before performing FVM-DSMC-ML simulations for conserved and non-conserved properties, we compare non-conserved properties estimated by the DNN model with the actual DSMC results. Figures 13, 14, 15, and 16 present comparisons of viscous stress, translational heat flux,

rotational heat flux, and vibrational heat flux for Mach numbers 4 and 8.5, respectively. The results predicted by the DNN model are in excellent agreement with the actual DSMC results.

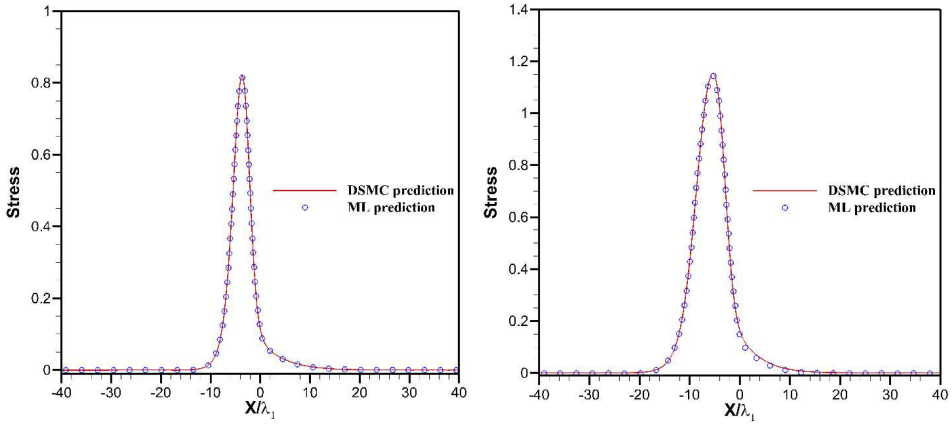

(a) M = 4 (b) M = 8.5

FIG. 13. Comparison of viscous stress profiles predicted by the DNN model and DSMC method for Mach numbers: (a) 4 and (b) 8.5. The DNN model here is trained using DSMC data from Mach numbers 4, 5, 6, 7, 8, 9, and 10.

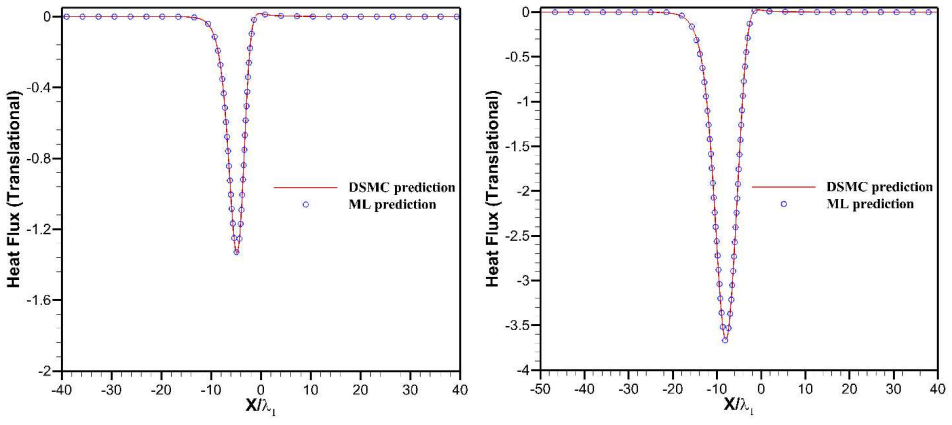

(a) M = 4 (b) M = 8.5

FIG. 14. Comparison of translational heat flux profiles predicted by the DNN model and the DSMC method for Mach numbers: (a) 4 and (b) 8.5. The DNN model is trained using DSMC data from Mach numbers 4, 5, 6, 7, 8, 9, and 10.

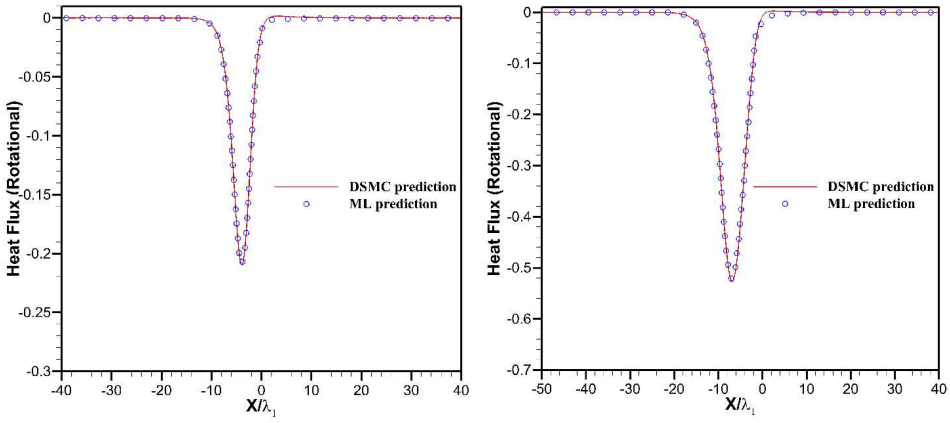

(a) M = 4 (b) M = 8.5

FIG. 15. Comparison of rotational heat flux profiles predicted by the DNN model (trained using DSMC data from Mach numbers 4, 5, 6, 7, 8, 9, and 10) and the DSMC method for Mach numbers: (a) 4 and (b) 8.5.

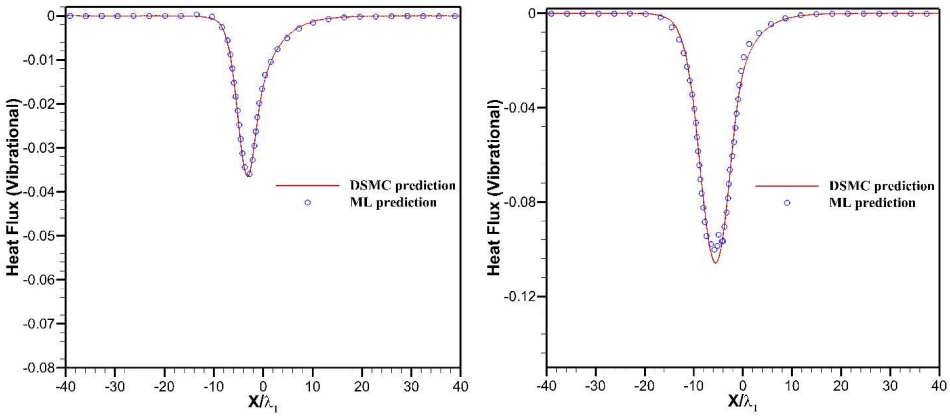

(a) M = 4 (b) M = 8.5

FIG. 16. Comparison of vibrational heat flux profiles predicted by the DNN model (trained using DSMC data from Mach numbers 4, 5, 6, 7, 8, 9, and 10) and the DSMC method for Mach numbers: (a) 4 and (b) 8.5.

Gimelshein, Gimelshein, and Levin [91] established a relationship between the vibrational relaxation ($Z_{V-T,DSMC}$) employed in DSMC and the corresponding value ($Z_{V-T,CFD}$) used in continuum-based CFD simulations. In the present study, we chose, however, not to use this relationship because we are directly implementing the DSMC fluxes into the conservation laws for the three-temperature framework (11). Here, a formulation, $Z_{V-T,FVM-DSMC-ML} = 1.2 Z_{V-T,DSMC}$, enables an effective resolution of the non-equilibrium between the translational and vibrational degrees of freedom through the inclusion of the Landau-Teller [60, 66] source term, as presented in equations (11). This approach aligns with the rationale detailed in Sec. III A of the two-temperature framework. The viscous stress and heat fluxes provided to the conservation laws account for non-equilibrium effects embedded in the DSMC solutions, and this vibrational heat flux stems from the vibrational relaxation process inherent to DSMC. Regarding

the Jeans source term [69], which calculates the energy exchange between the rotational and translational degrees of freedom, we employ the relation $Z_{R\text{-}T,FVM\text{-}DSMC\text{-}ML} = 1.2Z_{R\text{-}T,DSMC}$ as done in Sec. III A.

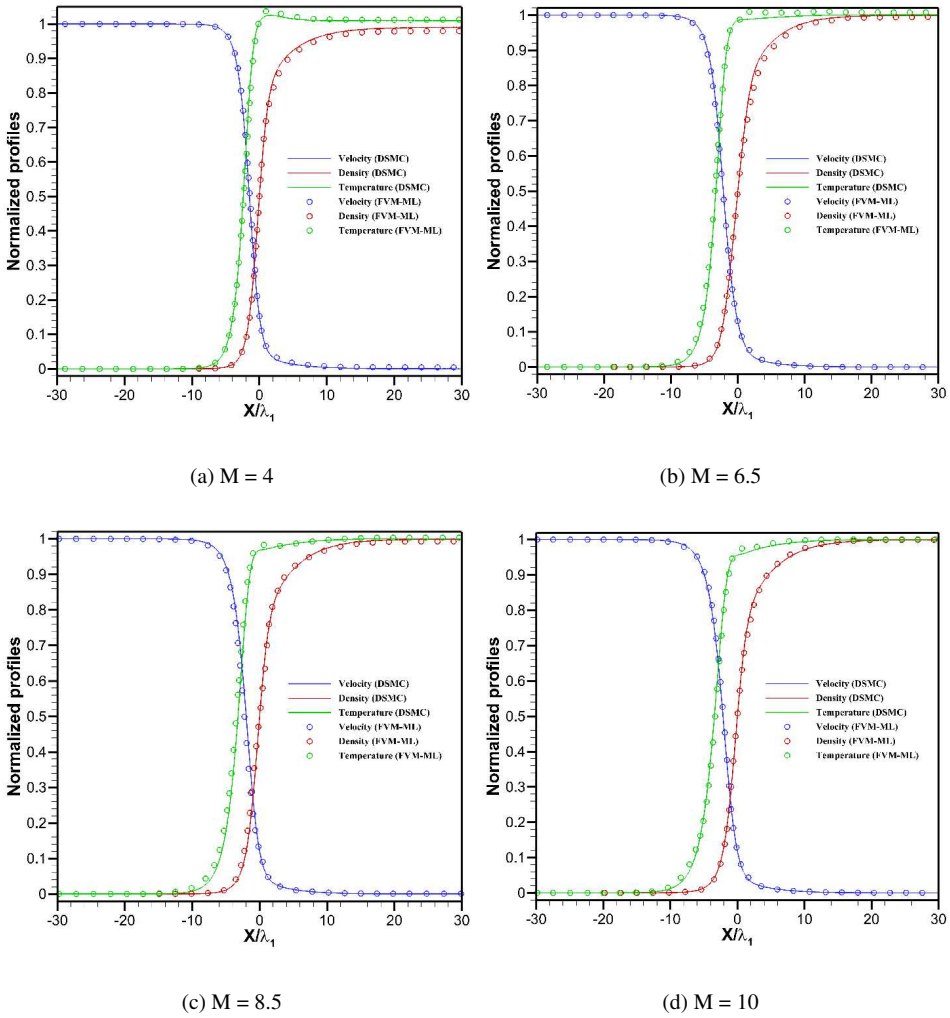

(a) M = 4 (b) M = 6.5

(c) M = 8.5 (d) M = 10

FIG. 17. Comparison of normalized conserved properties (density, velocity, and total temperature) of the FVM-DSMC-ML (three-temperature) and DSMC solutions for Mach numbers: (a) 4, (b) 6.5, (c) 8.5, and

(d) 10. The DNN model here is trained using DSMC data from Mach numbers 4, 5, 6, 7, 8, 9, and 10.

Figure 17 compares the normalized conserved properties (density, velocity, and total temperature) of the FVM-DSMC-ML (three-temperature) and DSMC solutions for four distinct cases, Mach numbers of 4, 6.5, 8.5, and 10. The main objective of this study was to develop an FVM solver capable of predicting the DSMC-equivalent non-equilibrium among the translational, rotational, and vibrational internal degrees of freedom. For this purpose, Fig. 18 compares the normalized properties (translational, rotational, and vibrational temperatures) of the FVM-DSMC-ML (three-temperature) and DSMC solutions.

Additionally, for completeness, we compare normalized thermophysical properties, specifically the specific heat ratio (γ) normalized using equation (21) and vibrational degrees of freedom (V_{DOF}) normalized using equation (20), with the actual DSMC solutions for Mach numbers of 4, 6.5, 8.5, and 10. Figures 17, 18, and 19 demonstrate that the FVM-DSMC-ML solver provides results that are in close agreement with the actual DSMC solutions.

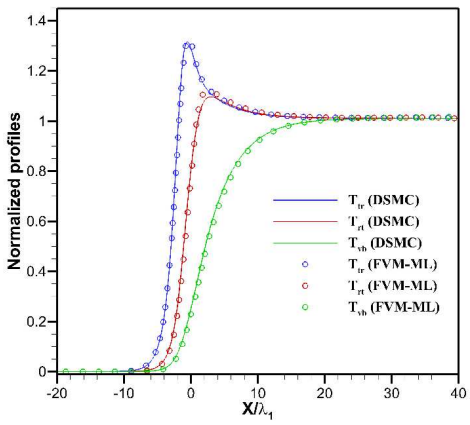

(a) M = 4

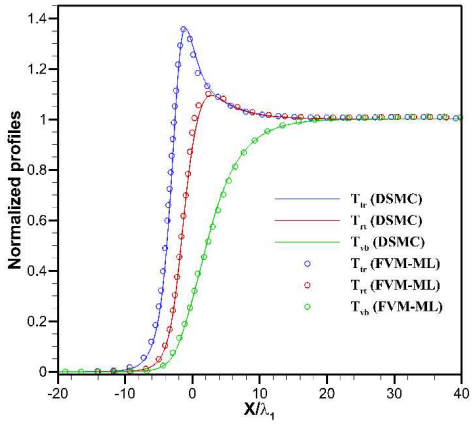

(b) M = 6.5

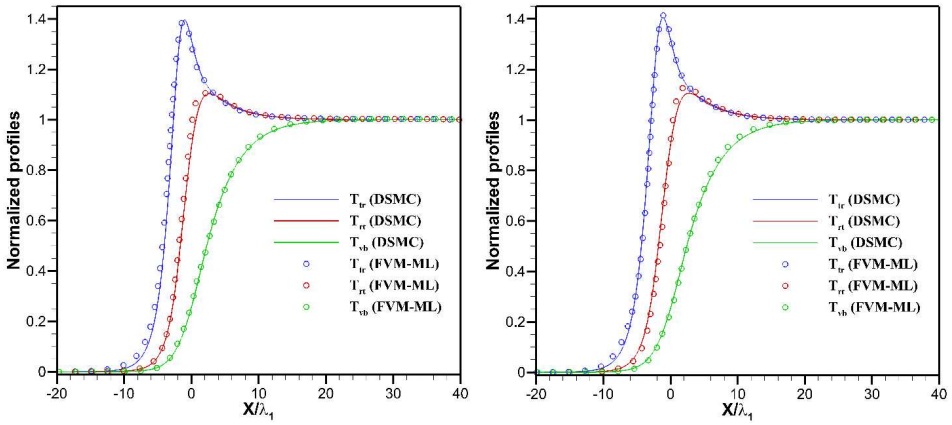

(c) M = 8.5 (d) M = 10

FIG. 18. Comparison of normalized properties (translational, rotational, and vibrational temperatures) of the FVM-DSMC-ML (three-temperature) and DSMC solutions for Mach numbers: (a) 4, (b) 6.5, (c) 8.5, and (d) 10. The DNN model here is trained using DSMC data from Mach numbers 4, 5, 6, 7, 8, 9, and 10.

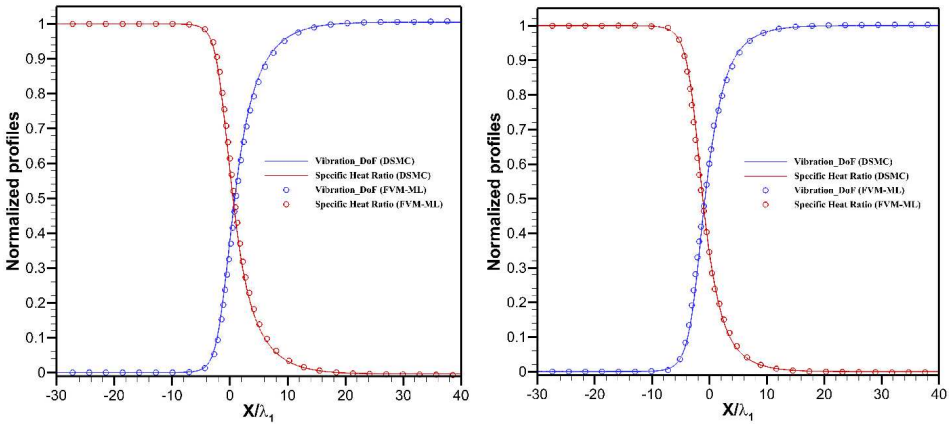

(a) M = 4 (b) M = 6.5

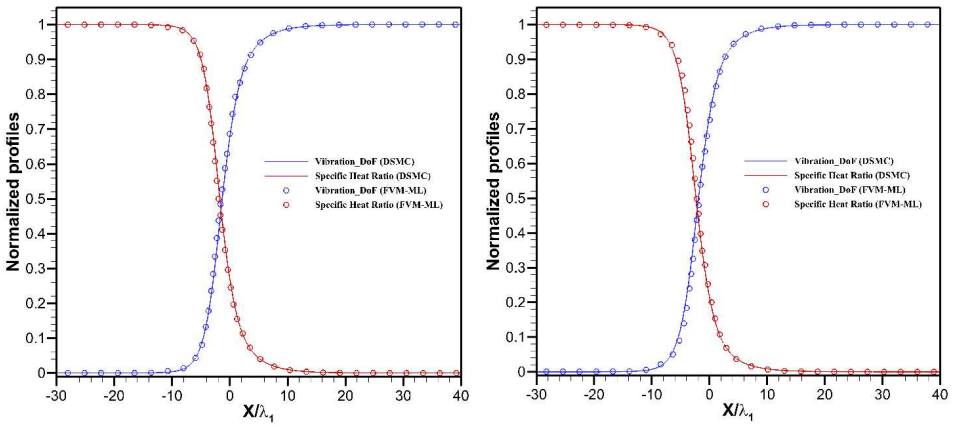

(c) M = 8.5 (d) M = 10

FIG. 19. Comparison of normalized properties (specific heat ratio and vibrational degrees of freedom) of the FVM-DSMC-ML (three-temperature) and DSMC solutions for Mach numbers: (a) 4, (b) 6.5, (c) 8.5, and (d) 10. The DNN model here is trained using DSMC data from Mach numbers 4, 5, 6, 7, 8, 9, and 10.

When evaluating the computational cost of the FVM-DSMC-ML solver compared to the two standard solvers, namely FVM-NSF and DSMC, the FVM-DSMC-ML solver is found to be approximately 1.2 to 1.5 times slower than the FVM-NSF solver. However, compared to the DSMC solver, the FVM-DSMC-ML solver shows superior performance with its computational cost being only 1/50 of that of the conventional DSMC solver. The cost of training the machine learning model—excluding the expense of generating the training DSMC dataset—is incurred only once, as it pertains to the construction of an *a priori* model. This cost is relatively modest, amounting to approximately $1/15^{th}$ of the computational resources needed to perform a simulation of a high Mach number 1D shock structure using the FVM-NSF solver.

IV. TOPOLOGY OF THE DSMC CONSTITUTIVE RELATIONS

Topology is a mathematical concept useful for describing the properties of a system that remains invariant under continuous transformations. Exploring the topological aspects of fluid dynamics has proven highly effective for characterizing fluid flows with complex physical behavior. A core idea in topology is that knowledge of objects is independent of their spatial embedding. In fluid dynamics, topological frameworks can be organized into various categories, including vortex and helicity [92], stability in dynamical systems, phase transitions, and constitutive relations [60, 74, 93]. For instance, the topology of vortex and helicity offers essential insights into the tendency of flows in classical fluids to form vortices or coherent structures. The constitutive relations in a topological form—the generic property of fluid—are transferable to all flow scenarios in principle because they describe the thermo-fluidic behavior of a fluid subjected to certain thermodynamic driving forces such as spatial gradients of velocity and temperature [93]. Therefore, when they are combined with the physical conservation laws of mass, momentum, energy, and initial and boundary conditions, any flow problem can be described within the limits of certain constitutive relations.

Garg *et al.* [1] presented the topology of the DSMC constitutive relations for the compressive flow branch in monatomic gases. Here we extend their work to diatomic gases, specifically presenting the DSMC topology for compressive flow in nitrogen. This is accomplished by developing two distinct multi-temperature FVM-DSMC-ML frameworks: a two-temperature model that incorporates translational and rotational internal energies, and a three-temperature model that additionally includes vibrational internal energy.

A. The two-temperature model with rotational degrees of freedom only

We first present the topology of the DNN-based DSMC constitutive relations (18) for the two-temperature framework given in (17). Figure 19 presents three-dimensional topologies (original DSMC, DNN-based DSMC model, and NSF) for the shock structure solutions, focusing on the compressive flow regime primarily characterized by positive viscous stress and negative heat fluxes. Variables carrying the

subscript '0' denote the corresponding values based on the NSF constitutive relations computed using equations (12)-(15).

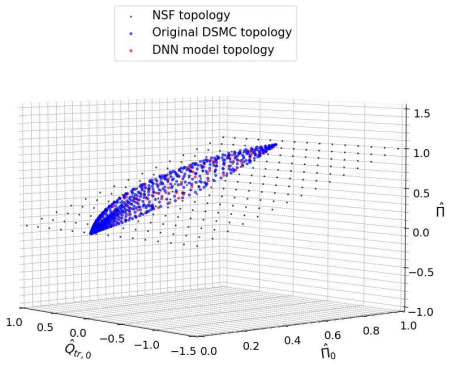

(a) 3D topology of viscous stress ($\hat{\mathbf{\Pi}}$)

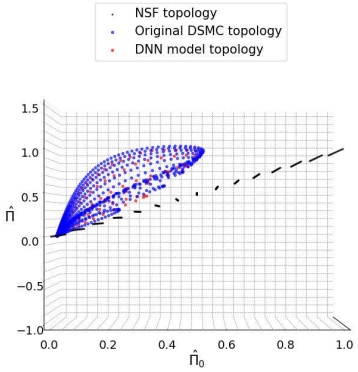

(b) 2D projection of viscous stress ($\hat{\mathbf{\Pi}}$)

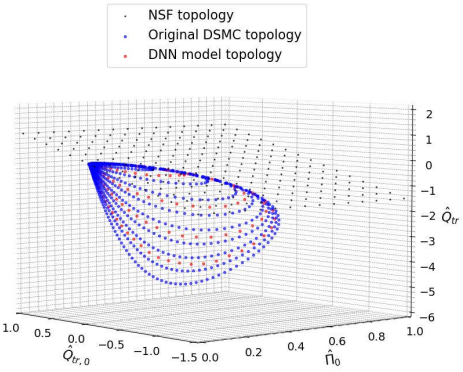

(c) 3D topology of translational heat flux ($\hat{\mathbf{Q}}_{\mathrm{tr}}$)

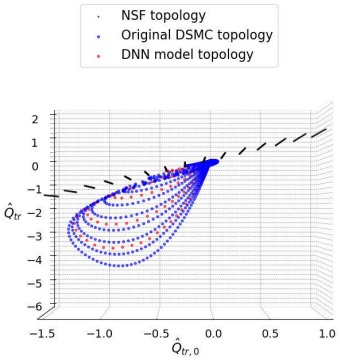

(d) 2D projection of translational heat flux ($\hat{\mathbf{Q}}_{\mathrm{tr}}$)

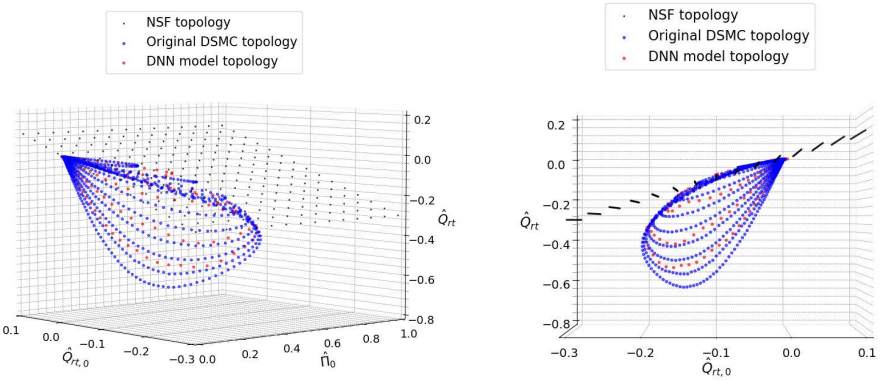

(e) 3D topology of rotational heat flux ($\hat{\mathbf{Q}}_{\mathrm{rt}}$) (f) 2D projection of rotational heat flux ($\hat{\mathbf{Q}}_{\mathrm{rt}}$)

FIG. 20. Comparison of topologies of the DSMC constitutive relations and the DNN-based model for the two-temperature case: (a) 3D topology of viscous stress, (b) 2D projection of the viscous stress topology on ($\hat{\Pi}_0, \hat{\Pi}$), (c) 3D topology of translational heat flux, (d) 2D projection of the translational heat flux topology on($\hat{\mathrm{Q}}_{tr,0}, \hat{\mathrm{Q}}_{tr}$), (e) 3D topology of rotational heat flux, and (f) 2D projection of the rotational heat flux topology on ($\hat{\mathrm{Q}}_{rt,0}, \hat{\mathrm{Q}}_{rt}$).

In Figs. 20(a), 20(c) and 20(e), the *x*-, *y*-, and *z*-axes correspond to the normalized hat quantities($\hat{\Pi}_0$, $\hat{\mathrm{Q}}_{tr,0}, \hat{\Pi}$), ($\hat{\Pi}_0, \hat{\mathrm{Q}}_{tr,0}, \hat{\mathrm{Q}}_{tr}$), and ($\hat{\Pi}_0, \hat{\mathrm{Q}}_{rt,0}, \hat{\mathrm{Q}}_{rt}$), respectively, defined in (10). In these figures, the blue symbols represent the topology of the original DSMC data for the Mach numbers used to train the DNN model (see Sec. III A), while the red symbols represent the DNN-based DSMC topology for intermediate Mach numbers not included in the training data. Figures 20(b), 20(d), and 20(f) present two-dimensional projections: viscous stress topology on the ($\hat{\Pi}_0, \hat{\Pi}$) plane, translational heat flux topology on the ($\hat{\mathrm{Q}}_{tr,0}$, $\hat{\mathrm{Q}}_{tr}$) plane, and rotational heat flux topology on the ($\hat{\mathrm{Q}}_{rt,0}, \hat{\mathrm{Q}}_{rt}$) plane, respectively.

A close look at these topologies reveals pronounced nonlinearities and strong coupling between viscous stresses and heat fluxes. The coupling is evident in the curvature along the direction of thermal forces at fixed viscous stress force values, particularly in cases where the flow significantly deviates from LTE (indicated as the origin). While the viscous stress primarily responds to the viscous stress force, it also varies nonlinearly with thermal force. In contrast, the NSF topology, represented by black symbols, shows a decoupled response to viscous stress and thermal forces, i.e., the viscous stress depends only on the viscous stress force, independent of thermal effects, and vice versa for the heat fluxes (both translational and rotational). Further, despite their nonlinearity, the DSMC and DNN-based DSMC topologies are smooth. Interestingly, in most regimes, the DSMC and DNN-based DSMC topologies exhibit higher values of viscous stress and translational heat flux compared to the NSF topology.

These topologies provide valuable insights into the flow regime that requires additional data to develop improved DNN models. A close look at the topology of the viscous stress reveals wider spacing between the DSMC topology curves at low Mach numbers (i.e., below Mach 5), suggesting that more data in this range would enhance the DNN's ability to accurately model the viscous stress. In addition, examining the DSMC heat flux magnitudes—whether translational or rotational—reveals significant variation with Mach number (e.g., the peak heat flux for Mach number 2 is approximately one-tenth of that for Mach number 10). This disparity indicates that insufficient data in lower Mach number regions may lead to unrealistic results, potentially degrading solution quality in those zones.

Compared to the monoatomic gas counterpart (as presented in Garg *et al.* [1]), we find that the transitional heat flux topology of the diatomic gas changes signs, i.e., becomes positive in certain regions downstream of the shock wave. As a result, the curves drawn for different Mach numbers intersect each other. This behavior can be attributed to the change in the slope of the translational temperature following the peak, as illustrated in Fig. 11. Interestingly, the predominant regions of the original and DNN-based DSMC rotational heat flux topologies for Mach numbers below 4 are smaller than those predicted by the NSF topology, as shown in Figs. 20 (e) and (f).

B. The three-temperature model with both rotational and vibrational degrees of freedom

We now present the topology of the DNN-based DSMC constitutive relations (7) for the three-temperature framework given in (11). Figure 21 presents three-dimensional topologies (original DSMC, DNN-based DSMC model, and NSF) of the shock structure solutions, focusing on the compressive flow regime, which is mostly characterized by positive viscous stress and heat fluxes with either positive or negative signs. Variables carrying the subscript '0' are computed using (12)-(15). These topologies represent a novel contribution to the understanding of shock wave structures.

In Figs. 21(a), 21(c), 21(e) and 21(g), the *x*-, *y*-, and *z*-axes correspond to the normalized hat quantities $(\hat{\Pi}_0, \hat{Q}_{tr,0}, \hat{\Pi})$, $(\hat{\Pi}_0, \hat{Q}_{tr,0}, \hat{Q}_{tr})$, and $(\hat{\Pi}_0, \hat{Q}_{rt,0}, \hat{Q}_{rt})$ and $(\hat{\Pi}_0, \hat{Q}_{vb,0}, \hat{Q}_{vb})$, respectively, defined in (10). In these figures, the blue symbols represent the topology of the original DSMC data for Mach numbers included in training the DNN model (see Sec. III B), while the red symbols represent the DNN-based DSMC topology for intermediate Mach numbers not included in the training data. The NSF topology is represented by the black symbols. Figures 21(b), 21(d), 21(f), and 21(h) present two-dimensional projections: viscous stress topology on the $(\hat{\Pi}_0, \hat{\Pi})$ plane, translational heat flux topology on the $(\hat{Q}_{tr,0}, \hat{Q}_{tr})$ plane, rotational heat flux topology on the $(\hat{Q}_{rt,0}, \hat{Q}_{rt})$ plane, and vibrational heat flux topology on the $(\hat{Q}_{vb,0}, \hat{Q}_{vb})$ plane, respectively.

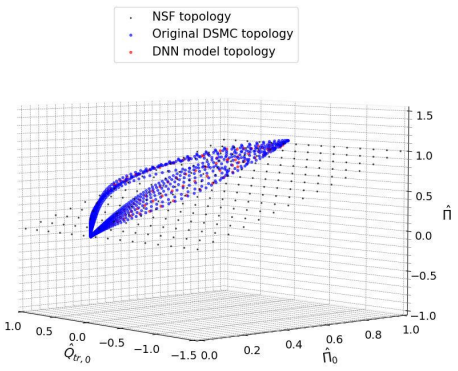

(a) 3D topology of viscous stress ($\hat{\mathbf{\Pi}}$)

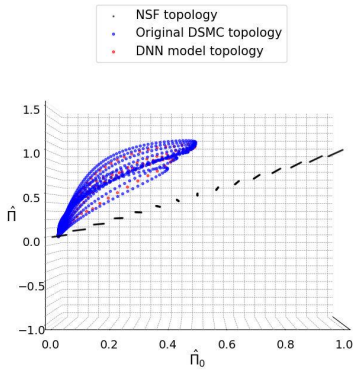

(b) 2D projection of viscous stress ($\hat{\mathbf{\Pi}}$)

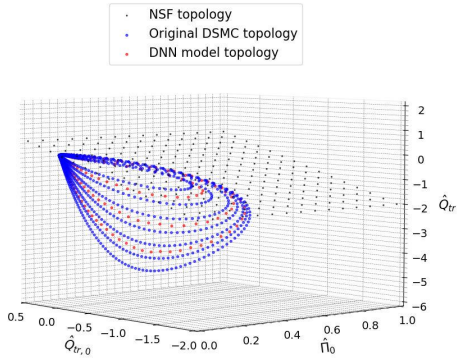

(c) 3D topology of translational heat flux ($\hat{\mathbf{Q}}_{\mathrm{tr}}$)

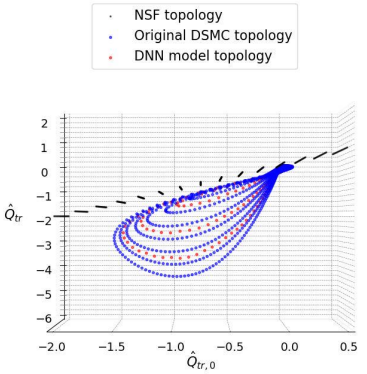

(d) 2D projection of translational heat flux ($\hat{\mathbf{Q}}_{\mathrm{tr}}$)

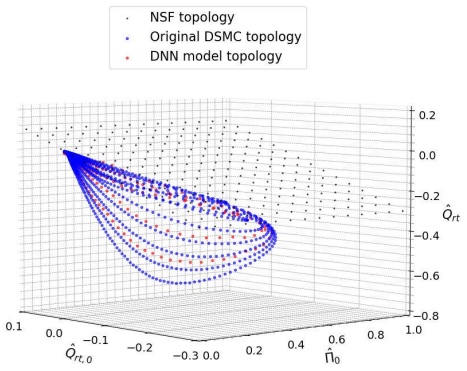

(e) 3D topology of rotational heat flux ($\hat{\mathbf{Q}}_{\mathrm{rt}}$)

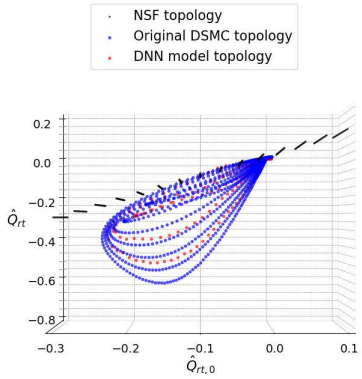

(f) 2D projection of rotational heat flux ($\hat{\mathbf{Q}}_{\mathrm{rt}}$)

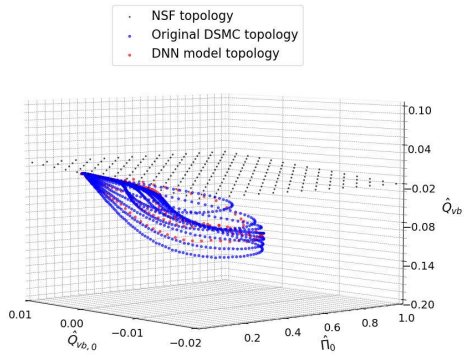

(g) 3D topology of vibrational heat flux ($\hat{\mathbf{Q}}_{\mathrm{vb}}$)

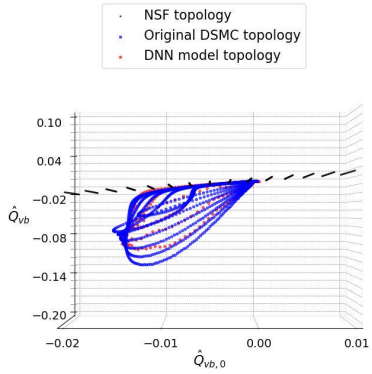

(h) 2D projection of vibrational heat flux ($\hat{\mathbf{Q}}_{\mathrm{vb}}$)

FIG. 21. Comparison of topologies of the DSMC constitutive relations and the DNN-based model for the three-temperature case: (a) 3D topology of viscous stress, (b) 2D projection of the viscous stress topology onto the ($\hat{\Pi}_0, \hat{\Pi}$) plane, (c) 3D topology of translational heat flux, (d) 2D projection of the translational heat flux topology onto the ($\hat{Q}_{tr,0}, \hat{Q}_{tr}$) plane, (e) 3D topology of rotational heat flux, (f) 2D projection of

the rotational heat flux topology onto the ($\hat{Q}_{rt,0}$, $\hat{Q}_{rt}$) plane, (g) 3D topology of vibrational heat flux, and (h) 2D projection of the vibrational heat flux topology onto the ($\hat{Q}_{vb,0}$, $\hat{Q}_{vb}$) plane.

Like the two-temperature model with rotational degrees of freedom only, as described in Sec. IV A, the topologies of the three-temperature framework exhibit pronounced nonlinearities and strong coupling between viscous stresses and heat fluxes. In addition, for the most part, the DSMC and DNN-based DSMC topologies exhibit higher values of viscous stress and heat fluxes compared to the NSF topology.

A close examination of the DSMC translational and rotational heat flux magnitudes reveals substantial variation with Mach number, with the peak heat flux for Mach number 4 being approximately one-fourth of that for Mach number 10. Further, the DSMC vibrational heat flux topology shows an intriguing pattern: in the upstream region, the vibrational heat flux profile varies as a multiple of the characteristic vibrational temperature, resulting in a series of Mach numbers with consistent topological shapes. These observations suggest that insufficient data in certain Mach number ranges could result in inaccurate model predictions, potentially compromising solution quality in these regions.

Compared to the topology of the rotational heat flux of the two-temperature framework described in Sec. IV A (where vibrational degrees of freedom are inactive), we find that the nearly equal spacing in magnitude between successive Mach numbers, noted in Sec. IV A, does not exist in the present three-temperature framework. The series of sets generated by multiples of the characteristic temperature in the vibrational heat flux affects the topology of rotational heat flux and exhibits similar characteristics. This is not observed in the translational heat flux, which can be attributed to the fact that the magnitude of translational heat flux for any Mach number is at least 2 orders of magnitude greater than the vibrational heat flux. In contrast, the rotational heat flux for a specific Mach number is quite close to that of its vibrational counterpart.

To summarize from Secs. IV A and IV B, it is clear that although both DSMC and NSF obey the same physical conservation laws, the essential differences observed between the DSMC and NSF topologies—

in particular, pronounced nonlinearities and strong coupling between viscous stresses and heat fluxes—are responsible for the different shock structure profiles observed in the DSMC and NSF solutions.

V. CONCLUDING REMARKS

The objective of this study is to extend the FVM-DSMC-ML framework to diatomic gases with vibrational modes by employing the two-temperature framework (translational and rotational) as well as the three-temperature framework (translational, rotational, and vibrational). The core idea of this framework is to combine DNN-based DSMC constitutive relations with traditional CFD codes, such as FVM or discontinuous Galerkin (DG) methods, to establish a third approach for describing gas flows including rarefied and microscale gases, complementing existing PDE-based and purely particle-based methods. In this framework, DNN-ML models serve to construct constitutive relations from computationally simulated data in a multi-variable space for fundamental flow regimes which establish a foundation applicable to diverse flow problems. Accordingly, the present DNN-ML models provide an alternative to the traditional methods of deriving constitutive relations from experimental data or empirical techniques.

In principle, the approach presented in this study can extend beyond the DSMC framework to encompass molecular dynamics (MD) and gas kinetic solvers (GKSs), where explicit forms of PDEs for constitutive relations are often lacking. This is possible because the method is based on the concept that constitutive relations independent of spatial embedding (thus called topology) can be first derived from raw simulated spatial flow data that satisfy physical conservation laws, and then later combined separately with an external computational solver for the conservation laws. This opens the possibility of developing various FVM-ML solvers, including FVM-MD-ML and FVM-GKS-ML.

We considered the one-dimensional shock wave structure, focusing on diatomic gas (specifically nitrogen), which is a well-studied problem in the context of nonequilibrium gas flow. We subsequently developed a single DNN model from the DSMC solution data alongside the associated FVM-DSMC-ML solver, capable of providing solutions for arbitrary Mach numbers with computational efficiency

comparable to that of the FVM-NSF solver. The simulation results indicated an acceptable equivalence between the FVM-DSMC-ML and DSMC solutions. Additionally, we constructed the topology of the DSMC constitutive relations for diatomic gas for the first time, enabling us to investigate how the DSMC topology deviates from the NSF topology in regions where the flow is significantly removed from LTE.

The current DNN-based FVM-DSMC-ML solver represents an innovative approach with significant potential; however, several challenges must be addressed to establish it as a robust method capable of tackling real-world scientific and technical problems. First, the method should be extendable to accommodate high-temperature gas flows involving chemical reactions [7, 24, 71, 94] and unsteady flow phenomena. At the same time, in the long term, it should be expanded toward developing quantum algorithms [95] capable of solving shock structure problems using quantum computing. Second, in addition to the compressive flow branch of the constitutive relations topology examined in this study, it is essential to develop additional machine learning models for other flow regimes, including expansion and boundary-driven velocity shear. Finally, it should be developed to address the challenges of multi-dimensional flows, going beyond the one-dimensional framework developed in this study. We hope to report our progress on these topics in due course.

ACKNOWLEDGEMENTS

This work was supported by the US AFOSR Grant No. FA2386-22-1-4051.

AUTHOR DECLARATIONS

Conflict of Interest

The authors have no conflicts to disclose.

DATA AVAILABILITY

The data that support the findings of this study are available from the corresponding authors upon reasonable request.

REFERENCES

[1] G. Garg, T.K. Mankodi, E. Esmaeilifar, R.S. Myong, Neural network-based finite volume method and direct simulation Monte Carlo solutions of non-equilibrium shock flow guided by nonlinear coupled constitutive relations, Physics of Fluids, 36(10) (2024) 106113.
[2] J.D. Anderson, Hypersonic and High-temperature Gas Dynamics, American Institute of Aeronautics and Astronautics, 2006.
[3] W.G. Vincenti, C.H. Kruger, Introduction to Physical Gas Dynamics, Wiley, 1965.
[4] G. Herzberg, Molecular Spectra and Molecular Structure, Read Books, 2007.
[5] C. Park, Nonequilibrium Hypersonic Aerothermodynamics, Wiley, 1990.
[6] J.G. Kim, G. Park, Thermochemical nonequilibrium parameter modification of oxygen for a two-temperature model, Physics of Fluids, 30(1) (2018) 016101.
[7] T.K. Mankodi, R.S. Myong, Quasi-classical trajectory-based non-equilibrium chemical reaction models for hypersonic air flows, Physics of Fluids, 31(10) (2019) 106102.
[8] T.K. Mankodi, R.S. Myong, Erratum: "Quasi-classical trajectory-based non-equilibrium chemical reaction models for hypersonic air flows" [Phys. Fluids 31, 106102 (2019)], Physics of Fluids, 32(1) (2020) 019901.
[9] G.V. Candler, I. Nompelis, Computational fluid dynamics for atmospheric entry, Non-Equilibrium Dynamics: From Physical Models to Hypersonic Flights; The von Karman Institute for Fluid Dynamics: Rhode-Saint-Genèse, Belgium, (2009).
[10] Z. Jiang, W. Zhao, Z. Yuan, W. Chen, R.S. Myong, Computation of hypersonic flows over flying configurations using a nonlinear constitutive model, AIAA Journal, 57(12) (2019) 5252-5268.
[11] S. Singh, A. Karchani, T. Chourushi, R.S. Myong, A three-dimensional modal discontinuous Galerkin method for the second-order Boltzmann-Curtiss-based constitutive model of rarefied and microscale gas flows, Journal of Computational Physics, 457 (2022) 111052.
[12] K. Vogiatzis, A. Munafò, M. Panesi, P. Vedula, E. Josyula, HyperCode: A framework for high-order accurate turbulent non-equilibrium hypersonic flow simulations, in: AIAA Scitech 2020 Forum.
[13] J. Zhang, Z. Wang, C.-Y. Liu, M. Sun, H. Wang, J. Ai, Numerical study of shock-induced thermochemical nonequilibrium effects in a high Mach flow field, Physics of Fluids, 36(9) (2024) 096128.
[14] G.V. Candler, P.K. Subbareddy, J.M. Brock, Advances in Computational Fluid Dynamics Methods for Hypersonic Flows, Journal of Spacecraft and Rockets, 52(1) (2015) 17-28.
[15] C. Kim, K.H. Kim, Y. Yang, J.G. Kim, Effect of multi-temperature models on heat transfer and electron behavior in hypersonic flows, Physics of Fluids, 36(9) (2024) 096127.
[16] G.A. Bird, Molecular Gas Dynamics and the Direct Simulation of Gas Flows, Clarendon Press, 1994.
[17] G.A. Bird, M.A. Gallis, J.R. Torczynski, D.J. Rader, Accuracy and efficiency of the sophisticated direct simulation Monte Carlo algorithm for simulating noncontinuum gas flows, Physics of Fluids, 21(1) (2009) 017103.
[18] A. Karchani, R.S. Myong, Convergence analysis of the direct simulation Monte Carlo based on the physical laws of conservation, Computers & Fluids, 115 (2015) 98-114.
[19] R.S. Myong, A. Karchani, O. Ejtehadi, A review and perspective on a convergence analysis of the direct simulation Monte Carlo and solution verification, Physics of Fluids, 31(6) (2019) 066101.
[20] S.K. Stefanov, On the basic concepts of the direct simulation Monte Carlo method, Physics of Fluids, 31(6) (2019) 067104.
[21] A. Alamatsaz, A. Venkattraman, Characterizing deviation from equilibrium in direct simulation Monte Carlo simulations, Physics of Fluids, 31(4) (2019) 042005.
[22] C. Borgnakke, P.S. Larsen, Statistical collision model for Monte Carlo simulation of polyatomic gas mixture, Journal of Computational Physics, 18(4) (1975) 405-420.
[23] I.D. Boyd, Analysis of vibrational-translational energy transfer using the direct simulation Monte Carlo method, Physics of Fluids A: Fluid Dynamics, 3(7) (1991) 1785-1791.

[24] G.A. Bird, The Q-K model for gas-phase chemical reaction rates, Physics of Fluids, 23(10) (2011) 106101.
[25] S.F. Gimelshein, I.J. Wysong, Bird's total collision energy model: 4 decades and going strong, Physics of Fluids, 31(7) (2019) 076101.
[26] I.D. Boyd, G. Chen, G.V. Candler, Predicting failure of the continuum fluid equations in transitional hypersonic flows, Physics of Fluids, 7(1) (1995) 210-219.
[27] T.E. Schwartzentruber, L.C. Scalabrin, I.D. Boyd, A modular particle–continuum numerical method for hypersonic non-equilibrium gas flows, Journal of Computational Physics, 225(1) (2007) 1159-1174.
[28] T.E. Schwartzentruber, I.D. Boyd, Progress and future prospects for particle-based simulation of hypersonic flow, Progress in Aerospace Sciences, 72 (2015) 66-79.
[29] J. Fan, C. Shen, Statistical simulation of low-speed rarefied gas flows, Journal of Computational Physics, 167(2) (2001) 393-412.
[30] H. Yang, J. Zhang, A theoretical framework of information preservation method and its application to low-speed nonequilibrium gas flows, Physics of Fluids, 35(7) (2023) 077121.
[31] P.L. Bhatnagar, E.P. Gross, M. Krook, A model for collision processes in gases. I. Small amplitude processes in charged and neutral one-component systems, Physical Review, 94(3) (1954) 511-525.
[32] E.M. Shakhov, Generalization of the Krook kinetic relaxation equation, Fluid Dynamics, 3(5) (1968) 95-96.
[33] L.H. Holway, Jr., New statistical models for kinetic theory: Methods of construction, Physics of Fluids, 9(9) (1966) 1658-1673.
[34] F. Fei, J. Zhang, J. Li, Z. Liu, A unified stochastic particle Bhatnagar-Gross-Krook method for multiscale gas flows, Journal of Computational Physics, 400 (2020) 108972.
[35] K. Feng, Z. Cui, P. Tian, J. Zhang, A unified stochastic particle method with spatiotemporal adaptation for simulating multiscale gas flows, Journal of Computational Physics, 505 (2024) 112915.
[36] M.H. Gorji, M. Torrilhon, P. Jenny, Fokker–Planck model for computational studies of monatomic rarefied gas flows, Journal of Fluid Mechanics, 680 (2011) 574-601.
[37] K. Xu, X. He, C. Cai, Multiple temperature kinetic model and gas-kinetic method for hypersonic non-equilibrium flow computations, Journal of Computational Physics, 227(14) (2008) 6779-6794.
[38] X. Xu, Y. Chen, K. Xu, Modeling and computation for non-equilibrium gas dynamics: Beyond single relaxation time kinetic models, Physics of Fluids, 33(1) (2021) 011703.
[39] Y. Wei, Y. Zhu, K. Xu, Unified gas-kinetic wave-particle methods VII: Diatomic gas with rotational and vibrational nonequilibrium, Journal of Computational Physics, 497 (2024) 112610.
[40] M. Pfeiffer, Extending the particle ellipsoidal statistical Bhatnagar-Gross-Krook method to diatomic molecules including quantized vibrational energies, Physics of Fluids, 30(11) (2018) 116103.
[41] M.H. Gorji, P. Jenny, A Fokker–Planck based kinetic model for diatomic rarefied gas flows, Physics of Fluids, 25(6) (2013) 062002.
[42] D. Burnett, The distribution of molecular velocities and the mean motion in a non-uniform gas, Proceedings of the London Mathematical Society, s2-40(1) (1936) 382-435.
[43] J.M. Reese, L.C. Woods, F.J.P. Thivet, S.M. Candel, A second-order description of shock structure, Journal of Computational Physics, 117(2) (1995) 240-250.
[44] R.K. Agarwal, K.-Y. Yun, R. Balakrishnan, Beyond Navier–Stokes: Burnett equations for flows in the continuum–transition regime, Physics of Fluids, 13(10) (2001) 3061-3085.
[45] W. Zhao, W. Chen, R.K. Agarwal, Formulation of a new set of Simplified Conventional Burnett equations for computation of rarefied hypersonic flows, Aerospace Science and Technology, 38 (2014) 64-75.
[46] W. Zhao, W. Chen, R.K. Agarwal, Computation of rarefied hypersonic flows using modified form of conventional Burnett equations, Journal of Spacecraft and Rockets, 52(3) (2015) 789-803.
[47] H. Grad, On the kinetic theory of rarefied gases, Communications on Pure and Applied Mathematics, 2(4) (1949) 331-407.
[48] H. Grad, The profile of a steady plane shock wave, Communications on Pure and Applied Mathematics, 5(3) (1952) 257-300.

[49] M. Torrilhon, Two-dimensional bulk microflow simulations based on regularized Grad's 13-moment equations, Multiscale Modeling & Simulation, 5(3) (2006) 695-728.
[50] M. Torrilhon, Modeling nonequilibrium gas flow based on moment equations, Annual Review of Fluid Mechanics, 48 (2016) 429-458.
[51] B.C. Eu, Kinetic Theory and Irreversible Thermodynamics, Wiley, 1992.
[52] M. Al-Ghoul, B.C. Eu, Generalized hydrodynamics and shock waves, Physical Review E, 56(3) (1997) 2981-2992.
[53] R.S. Myong, Thermodynamically consistent hydrodynamic computational models for high-Knudsen-number gas flows, Physics of Fluids, 11(9) (1999) 2788-2802.
[54] R.S. Myong, A computational method for Eu's generalized hydrodynamic equations of rarefied and microscale gasdynamics, Journal of Computational Physics, 168(1) (2001) 47-72.
[55] R.S. Myong, A generalized hydrodynamic computational model for rarefied and microscale diatomic gas flows, Journal of Computational Physics, 195(2) (2004) 655-676.
[56] N.T.P. Le, H. Xiao, R.S. Myong, A triangular discontinuous Galerkin method for non-Newtonian implicit constitutive models of rarefied and microscale gases, Journal of Computational Physics, 273 (2014) 160-184.
[57] A. Rana, R. Ravichandran, J.H. Park, R.S. Myong, Microscopic molecular dynamics characterization of the second-order non-Navier-Fourier constitutive laws in the Poiseuille gas flow, Physics of Fluids, 28(8) (2016) 082003.
[58] O. Ejtehadi, R.S. Myong, I. Sohn, B.J. Kim, Full continuum approach for simulating plume-surface interaction in planetary landings, Physics of Fluids, 35(4) (2023) 043331.
[59] T.K. Mankodi, O. Ejtehadi, T. Chourushi, A. Rahimi, R.S. Myong, nccrFOAM suite: Nonlinear coupled constitutive relation solver in the OpenFOAM framework for rarefied and microscale gas flows with vibrational non-equilibrium, Computer Physics Communications, 296 (2024) 109024.
[60] T.K. Mankodi, R.S. Myong, Boltzmann-based second-order constitutive models of diatomic and polyatomic gases including the vibrational mode, Physics of Fluids, 32(12) (2020) 126109.
[61] J. Zhang, W. Ma, Data-driven discovery of governing equations for fluid dynamics based on molecular simulation, Journal of Fluid Mechanics, 892 (2020) A5.
[62] W. Ma, J. Zhang, K. Feng, H. Xing, D. Wen, Dimensional homogeneity constrained gene expression programming for discovering governing equations, Journal of Fluid Mechanics, 985 (2024) A12.
[63] C. Park, The limits of two-temperature kinetic model in air, AIAA Paper 2010-911, (2010).
[64] I.D. Boyd, E. Josyula, State resolved vibrational relaxation modeling for strongly nonequilibrium flows, Physics of Fluids, 23(5) (2011) 057101.
[65] J. Olejniczak, G.V. Candler, Vibrational energy conservation with vibration–dissociation coupling: General theory and numerical studies, Physics of Fluids, 7(7) (1995) 1764-1774.
[66] L. Landau, Theory of Sound Dispersion, Physikalische Zeitschrift der Sowjetunion, 10 (1936) 34-43.
[67] S.P. Sharma, W. Gillespie, Nonequilibrium and equilibrium shock front radiation measurements, Journal of Thermophysics and Heat Transfer, 5(3) (1991) 257-265.
[68] J.G. Kim, Rovibrational nonequilibrium of nitrogen behind a strong normal shock wave, International Journal of Aeronautical and Space Sciences, 18(1) (2017) 28-37.
[69] J. Jeans, The Dynamical Theory of Gases, 4 ed., Cambridge University Press, Cambridge, 2009.
[70] C. Park, Rotational relaxation of N2 behind a strong shock wave, Journal of Thermophysics and Heat Transfer, 18(4) (2004) 527-533.
[71] J.G. Kim, I.D. Boyd, State-resolved master equation analysis of thermochemical nonequilibrium of nitrogen, Chemical Physics, 415 (2013) 237-246.
[72] J.G. Kim, I.D. Boyd, Master equation analysis of post normal shock waves of nitrogen, Journal of Thermophysics and Heat Transfer, 29(2) (2015) 241-252.
[73] R.S. Myong, On the high Mach number shock structure singularity caused by overreach of Maxwellian molecules, Physics of Fluids, 26(5) (2014) 056102.

[74] H. Srivastava, T.K. Mankodi, R.S. Myong, Second-order constitutive relations and their topologies for rotational non-equilibrium in diatomic gas flows using a multi-temperature approach, Physics of Fluids, 37(3) (2025) 036154.
[75] J.D. Anderson, Modern Compressible Flow, with Historical Perspective, McGraw-Hill, 1982.
[76] R.S. Myong, Analytical solutions of shock structure thickness and asymmetry in Navier–Stokes/Fourier framework, AIAA Journal, 52(5) (2014) 1075-1081.
[77] M. Morduchow, P.A. Libby, On a complete solution of the one-dimensional flow equations of a viscous, heat-conducting, compressible gas, Journal of the Aeronautical Sciences, 16(11) (1949) 674-684.
[78] H.M. Mott-Smith, The solution of the Boltzmann equation for a shock wave, Physical Review, 82(6) (1951) 885-892.
[79] B. van Leer, Towards the ultimate conservative difference scheme, Journal of Computational Physics, 135(2) (1997) 229-248.
[80] E.F. Toro, M. Spruce, W. Speares, Restoration of the contact surface in the HLL-Riemann solver, Shock Waves, 4(1) (1994) 25-34.
[81] V. Casseau, R.C. Palharini, T.J. Scanlon, R.E. Brown, A two-temperature open-source CFD model for hypersonic reacting flows, Part One: Zero-Dimensional Analysis, Aerospace, 3(4) (2016) 45.
[82] V. Casseau, An Open-Source CFD Solver for Planetary Entry, University of Strathclyde, Glasgow, UK, 2017.
[83] D.P. Kingma, J. Ba, Adam: A method for stochastic optimization, ArXiv preprint arXiv:1412.6980, (2017).
[84] D.-A. Clevert, T. Unterthiner, S. Hochreiter, Fast and accurate deep network learning by exponential linear units (ELUs), ArXiv preprint arXiv:1511.07289, (2016).
[85] A.L. Maas, A.Y. Hannun, A.Y. Ng, Rectifier nonlinearities improve neural network acoustic models, in: Proceedings of the 30th International Conference on Machine Learning, Vol. 28, Atlanta, GA, 2013, pp. 3.
[86] D. Misra, Mish: A self regularized non-monotonic activation function, ArXiv preprint arXiv:1908.08681, (2020).
[87] F.E. Lumpkin, III, Development and evaluation of continuum models for translational-rotational nonequilibrium, Ph.D., Stanford University, United States, California, 1990.
[88] F.E. Lumpkin, III, B.L. Haas, I.D. Boyd, Resolution of differences between collision number definitions in particle and continuum simulations, Physics of Fluids A: Fluid Dynamics, 3(9) (1991) 2282-2284.
[89] H.-S. Tsien, One-dimensional flows of a gas characterized by van der Waal's equation of state, Journal of Mathematics and Physics, 25(1-4) (1946) 301-324.
[90] A.J. Eggers, One-dimensional flows of an imperfect diatomic gas, 959, National Advisory Committee for Aeronautics, 1949.
[91] N.E. Gimelshein, S.F. Gimelshein, D.A. Levin, Vibrational relaxation rates in the direct simulation Monte Carlo method, Physics of Fluids, 14(12) (2002) 4452-4455.
[92] H.K. Moffatt, G.M. Zaslavsky, P. Comte, M. Tabor, Topological Aspects of the Dynamics of Fluids and Plasmas, Springer Netherlands, 2013.
[93] S. Singh, A. Karchani, K. Sharma, R.S. Myong, Topology of the second-order constitutive model based on the Boltzmann–Curtiss kinetic equation for diatomic and polyatomic gases, Physics of Fluids, 32(2) (2020) 026104.
[94] S. Zeng, J. Yang, W. Zhao, Z. Yuan, G. Fan, W. Chen, Nonlinear coupled constitutive relations for hypersonic reacting flows with thermal nonequilibrium effect, Physics of Fluids, 37(1) (2025) 016116.
[95] E. Esmaeilifar, D. Ahn, R.S. Myong, Quantum algorithm for nonlinear Burgers' equation for high-speed compressible flows, Physics of Fluids, 36(10) (2024) 106110.